J. Mech. Phys. Solids 197 (2025) 105978

Contents lists available at ScienceDirect

Journal of the Mechanics and Physics of Solids

journal homepage: www.elsevier.com/locate/jmps

Phase field fracture in elastoplastic solids: a stress-state, strain-rate, and orientation dependent model in explicit dynamics and its applications to additively manufactured metals

Cunyi Li [a], Jian Liu [b], Le Dong [b], Chi Wu [c], Grant Steven [d], Qing Li [d], Jianguang Fang [a,*]

[a] School of Civil and Environmental Engineering, University of Technology Sydney, Sydney, NSW 2007, Australia
[b] Earthquake Engineering Research and Test Center, Guangzhou University, Guangzhou, 510405, China
[c] School of Engineering, University of Newcastle, Callaghan, NSW 2308, Australia
[d] School of Aerospace, Mechanical and Mechatronic Engineering, The University of Sydney, Sydney, NSW 2006, Australia

ARTICLE INFO

Keywords:
Phase field fracture
Additive manufacturing
Strain rate
Orientation dependency
Dynamic ductile fracture
TPMS structure

ABSTRACT

Phase field models have gained increasing popularity in analysing fracture behaviour of materials. However, few studies have been explored to simulate dynamic ductile fracture to date. This study aims to develop a phase field framework that considers strain rate, stress state, and orientation dependent ductile fracture under dynamic loading. Firstly, the governing equations of displacement and phase fields are formulated within an explicit finite element framework. Secondly, constitutive relations are established using a hypoelastic-plasticity framework, encompassing the influence of material orientation and strain rate on both plasticity and fracture initiation. Stress state dependent fracture initiation is also considered. Thirdly, the finite element implementation and corotational formulation of constitutive equations are derived. Finally, to validate the proposed model, additively manufactured samples, including material-level and crack propagation specimens, are tested under dynamic loading conditions. Overall, the proposed phase field model can properly reproduce the experimental force-displacement curves and crack paths. Uniaxial tension tests reveal that a higher strain rate can lead to a higher hardening curve and reduced ductility. Other material specimens further demonstrate the model's capability to predict stress state and orientation dependent dynamic fracture. To simulate dynamic crack paths accurately, it is necessary to consider anisotropic fracture initiation. Lastly, the phase field model was applied for the first time to predict the dynamic response of triply periodic minimal surface (TPMS) structures. Dynamic crack patterns were effectively captured, and the fracture mechanisms were thoroughly analysed. This study provides an explicit phase field framework for dynamic ductile fracture, with applications to additively manufactured materials and structures.

1. Introduction

The phase field fracture model has become widely favoured for its ability to effectively capture complex fracture phenomena, such as the nucleation, growth, branching, and merging of cracks (Wu et al., 2020; Zhuang et al., 2022). Its development can be traced back

* Corresponding author.
E-mail addresses: FangJG87@gmail.com, Jianguang.Fang@uts.edu.au (J. Fang).

https://doi.org/10.1016/j.jmps.2024.105978
Received 24 February 2024; Received in revised form 21 November 2024; Accepted 28 November 2024
Available online 3 December 2024

to the variational principle by Francfort and Marigo, 1998, and subsequent numerical implementation by Bourdin et al., 2000. Over the past two decades, extensive investigations have been conducted on the phase field approach in various fracture case scenarios, covering important topics such as brittle fracture (Ambati et al., 2014; Kumar et al., 2020; Lo et al., 2023; Wu and Nguyen, 2018), ductile fracture (Ambati et al., 2015; Huber and Asle Zaeem, 2023; Miehe et al., 2016), multi-field fracture (Dittmann et al., 2020; Hageman and Martínez-Pañeda, 2023; Miehe et al., 2015), erosion (Cui et al., 2021; Kristensen et al., 2020), multiaxial loading (Abrari Vajari et al., 2022; Wang et al., 2023), and dynamic fracture (Borden et al., 2012; Chu et al., 2019; Loew et al., 2019), demonstrating its compelling capability and extraordinary feature in fracture analysis (Zhuang et al., 2022).

Phase field models for dynamic fracture were developed from Ginzburg-Landau equation (Karma et al., 2001; Wu, 2017), and then derived by Bourdin-type formulation based on Griffith's theory (Borden et al., 2012) for engineering applications. Ren et al. (2019) proposed a simple, robust, and efficient explicit algorithm for the phase field model to address convergence issues encountered with implicit schemes. Weinberg and Wieners (2022) presented a wave induced dynamic fracture where the influence of wave superposition and reflections on fracture interfaces were also considered. Wang et al. (2019) incorporated the Mohr-Coulumb fracture criterion with an explicit phase field framework to capture shear damage of brittle materials. Shen et al. (2019) explored rate dependency for viscoelastic materials, indicating that the viscous energy had a significant influence on the damage growth rate at low strain rates but only a minor effect at high strain rates. Hofacker and Miehe (2013) developed a dynamic phase field model to capture impact velocity dependent crack patterns. To reduce computational cost, adaptive mesh refinement techniques (Gupta et al., 2022) and virtual modelling (Liu et al., 2023) have been explored for dynamic phase field fracture.

Nevertheless, the abovementioned phase field models mainly focused on dynamic brittle fracture. For dynamic ductile fracture, Hofacker and Miehe (2012b) developed a phase field approach for transition from ductile to brittle failure mode under dynamic loading. Molnár et al. (2020) reported that yield stress had a significant influence on fracture patterns. Chu et al. (2019) revealed that stress wave propagation was crucial in transition of brittle-ductile failure model. It should be pointed out that dynamic ductile fracture involves the effect of strain rate on plasticity and fracture initiation (Marandi et al., 2020; Xiao et al., 2019). The classical Johnson and Cook (1985) model and its extended forms (Pandya et al., 2020; Tang et al., 2021) have been extensively used to capture these influences. However, these models exhibit strong mesh dependency due to their localness, and thus unique solutions could not be achieved when encountering strain localisation (Pijaudier-Cabot et al., 1988).

For ductile fracture there is considerable plastic deformation prior to fracture initiation (Li et al., 2011). Therefore, a constant threshold was frequently used in the phase field fracture model to control non-physical damage at low levels of deformation (Miehe et al., 2015; Molnár et al., 2020). Recent studies (Abrari Vajari et al., 2022; Li et al., 2022a) have revealed that the threshold should depend on stress state (Bai and Wierzbicki, 2008), which can be characterised by stress triaxiality and the Lode angle parameter (see Section 3.2 for their definition) rather than a constant such that different crack behaviour under multiaxial loading could be captured. In the context of dynamic ductile fracture, Chu et al. (2019) assumed that shear fracture required a larger plastic deformation than tensile failure by introducing stress triaxiality dependent critical energy release rate. Nevertheless, the Lode angle parameter, another key variable to characterise the stress state, also significantly influences ductile fracture (Komori, 2021) in the regime of negative and low stress triaxiality cases (Wang et al., 2020).

In most of the abovementioned studies, plastic behaviour and fracture initiation were assumed to be isotropic. However, in real-life practice, anisotropic mechanical behaviour cannot be neglected for many materials such as conventional metal sheets (Banabic, 2010) and additively manufactured materials (Somlo et al., 2022; Wilson-Heid et al., 2020). To address this issue, Marandi et al. (2021) and Li et al. (2023) adopted the Hill48 plasticity model to capture conventional aluminium alloy and 3D-printed 316L steel, respectively. Furthermore, the anisotropic fracture initiation remains relatively unexplored, even in the case of typical metallic materials made of conventional manufacturing processes, primarily owing to the challenges associated with measurement of fracture strain (Lou and Yoon, 2017). Li et al. (2023) illustrated that anisotropic fracture initiation should be considered in the phase field model for quasi-static cases to predict the correct crack paths. Nonetheless, orientation dependency has not been studied in the phase field framework for dynamic fracture.

To sum up, phase field models for dynamic ductile fracture remain understudied, especially in terms of complex constitutive relations involving strain rate, stress state, and orientation dependencies. This study aims to bridge this knowledge gap. The remainder of this paper is structured as follows: Section 2 proposes an explicit phase field formulation in the explicit dynamics framework. Section 3 presents the hypoelastic-plasticity and fracture criteria for additively manufactured metallic materials. Section 4 presents spatial and temporal discretisation as well as an incrementally objective return mapping algorithm. Section 5 presents the experimental design and model calibration. Section 6 illustrates the effectiveness of the proposed models for dynamic ductile fracture involving global response, crack initiations and propagations. Section 7 summarises the key findings of this work.

2. Phase field model in explicit dynamics framework

In this section, a phase field fracture model in explicit dynamics is formulated in both weak and strong forms.

2.1. Energy functional

2.1.1. Total power

Consider an arbitrary elastoplastic body $\Omega \in \mathbb{R}^{dim}$ (where *dim* stands for the spatial dimension) with external boundary $\partial\Omega$ and internal discontinuity boundary Γ, as illustrated in Fig. 1a. Let $\partial\Omega^h$ and $\partial\Omega^s$ be the Dirichlet boundary and the Neumann boundary,

respectively, satisfying $\partial\Omega^h \cap \partial\Omega^s = \varnothing$ and $\partial\Omega = \overline{\partial\Omega^h \cup \partial\Omega^s}$. In the phase field framework, the sharp interface Γ is approximated in a diffusive form in terms of a phase field variable d ($0 \leq d \leq 1$), as illustrated in Fig. 1b. Here, $d = 0$ represents that the material remains intact, while $d = 1$ indicates a completely broken crack.

The regularised description of the crack functional in a multi-dimensional setting reads (Miehe et al., 2010b):

$$\Theta(d) = \int_\Omega \frac{1}{2l_c}\left(l_c^2 \nabla d \cdot \nabla d + d^2\right) \mathrm{d}\Omega, \tag{1}$$

where $\frac{1}{2l_c}\left(l_c^2 \nabla d \cdot \nabla d + d^2\right)$ defines the cracking surface density function per unit volume of the solid. Let g_f denote the energy required to create a unit area of the fracture surface, and then the fracture energy can be obtained as (Bourdin et al., 2008; Miehe et al., 2015):

$$E_{frac}(d) = \int_\Gamma g_f \mathrm{d}\Gamma \cong \int_\Omega \frac{g_f}{2l_c}\left(l_c^2 \nabla d \cdot \nabla d + d^2\right) \mathrm{d}\Omega. \tag{2}$$

The elastic power P_{elas} and plastic power P_{plas} at a given phase field state d (Hofacker and Miehe, 2012a) can be derived as:

$$P_{elas}(\mathbf{D}^e; d) = \int_\Omega (1-d)^2 \mathbf{D}^e : \widetilde{\boldsymbol{\sigma}} \, \mathrm{d}\Omega, \tag{3}$$

$$P_{plas}(\mathbf{D}^p; d) = \int_\Omega (1-d)^2 \mathbf{D}^p : \widetilde{\boldsymbol{\sigma}} \, \mathrm{d}\Omega = \int_\Omega (1-d)^2 (\mathbf{D} - \mathbf{D}^e) : \widetilde{\boldsymbol{\sigma}} \, \mathrm{d}\Omega. \tag{4}$$

Based on the plastic power equivalence (Simo and Hughes, 2006), the plastic power can also be expressed as:

$$P_{plas}(\dot{\bar{\varepsilon}}^p; d) = \int_\Omega (1-d)^2 \widetilde{f}(\widetilde{\boldsymbol{\sigma}}) \dot{\bar{\varepsilon}}^p \, \mathrm{d}\Omega = \int_\Omega f(\boldsymbol{\sigma}, d) \dot{\bar{\varepsilon}}^p \, \mathrm{d}\Omega. \tag{5}$$

In the above equations, $\mathbf{D}^e$ and $\mathbf{D}^p$ are elastic and plastic parts of deformation rate $\mathbf{D}$; $\dot{\bar{\varepsilon}}^p$ represents the equivalent plastic strain rate. $\widetilde{\boldsymbol{\sigma}}$ is the undamaged stress with "$\widetilde{\blacksquare}$" denoting the quantities in an undamaged configuration. For instance, $\widetilde{f}$ and f denote undamaged and damaged equivalent stress, respectively.

The kinetic power P_{kin} at a given acceleration $\dot{\mathbf{v}}$ is given as:

$$P_{kin}(\mathbf{v}; \dot{\mathbf{v}}) = \int \rho \mathbf{v} \cdot \dot{\mathbf{v}} \mathrm{d}\Omega, \tag{6}$$

where "$\dot{\blacksquare}$" denotes a time rate, $\mathbf{v}$ and $\dot{\mathbf{v}}$ denote the velocity and acceleration fields, respectively, ρ is the mass density.

Using the divergence theorem and the integration-by-parts theorem, the fracture power at a given state d can be expressed as (Bourdin et al., 2008; Miehe et al., 2015):

$$P_{frac}(\dot{d}; d) = \frac{\mathrm{d}E_{frac}}{\mathrm{d}t} = \int_{\partial\Omega} \left(g_f l_c \mathbf{n} \cdot \nabla d \, \dot{d}\right) \mathrm{d}\partial\Omega - \int_\Omega \frac{g_f}{l_c}\left(l_c^2 \nabla^2 d \, \dot{d} - d\dot{d}\right) \mathrm{d}\Omega, \tag{7}$$

To be compatible with an explicit finite element framework (Ziaei-Rad and Shen, 2016), the viscous power $P_{vis}(\dot{d})$ can be given as (Zhang et al., 2022):

$$P_{vis}(\dot{d}) = \int_\Omega \frac{\omega}{2} \dot{d} \cdot \dot{d} \, \mathrm{d}\Omega, \tag{8}$$

where ω is the artificial viscosity parameter. The external power can be derived as:

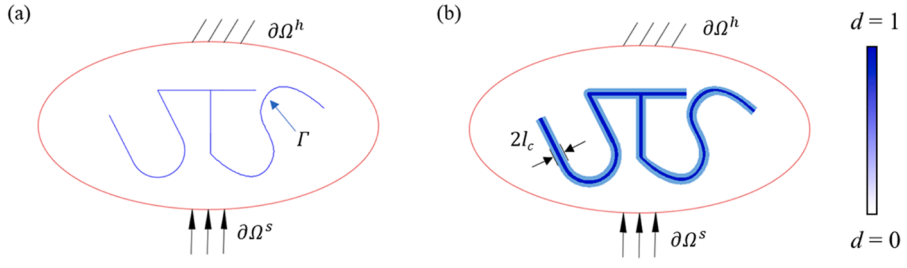

Fig. 1. Crack morphology of a solid with Dirichlet boundary $\partial\Omega^h$ and Neumann boundary $\partial\Omega^s$ over a time period $[0, t]$. (a) Sharp representation of interfacial discontinuity Γ; (b) Diffusive crack represented by a phase field variable d with a length scale parameter l_c to represent the crack width.

$$P_{ext}(\mathbf{v}) = \int_{\Omega} (\mathbf{f}\cdot\mathbf{v})\mathrm{d}\Omega + \int_{\partial\Omega^s} (\mathbf{t}\cdot\mathbf{v})\mathrm{d}\partial\Omega^s, \tag{9}$$

in which $\mathbf{f}$ and $\mathbf{t}$ are the body force and boundary traction, respectively. Finally, the total power functional can be expressed as:

$$\Pi(\mathbf{v},\ \dot{\bar{\varepsilon}}^p, \dot{d}) = P_{elas} + P_{plas} + P_{frac} + P_{vis} + P_{kin} - P_{ext}. \tag{10}$$

2.1.2. Weak form

Following the formulation of explicit dynamics (Belytschko et al., 2014; Miehe et al., 2015), the governing equation in a weak form for the displacement field can be derived as:

$$\int (1-d)^2\widetilde{\boldsymbol{\sigma}} : \delta\mathbf{D}\ \mathrm{d}\Omega + \int \rho\dot{\mathbf{v}}\cdot\delta\mathbf{v}\mathrm{d}\Omega\ - \int \mathbf{f}\cdot\delta\mathbf{v}\ \mathrm{d}\Omega - \int_{\partial\Omega^s} \mathbf{t}\cdot\delta\mathbf{v}\ \mathrm{d}\partial\Omega^s = 0. \tag{11}$$

where $\mathbf{D} = \partial\mathbf{v}/\partial\mathbf{x}$. Together with divergence theorem and integration by part, the above equation could be further transformed into

$$\int_{\partial\Omega^s} (\mathbf{n}\cdot\boldsymbol{\sigma} - \mathbf{t})\cdot\delta\mathbf{v}\ \mathrm{d}\partial\Omega^s - \int_{\Omega} (\mathrm{div}\ \boldsymbol{\sigma} + \mathbf{f} - \rho\dot{\mathbf{v}})\cdot\delta\mathbf{v}\ \mathrm{d}\Omega = 0. \tag{12}$$

The governing equation for the phase field is formulated as:

$$-\int_{\Omega} 2(1-d)\left(\int \widetilde{\boldsymbol{\sigma}} : \mathbf{D}\mathrm{d}t\right)\delta\dot{d}\mathrm{d}\Omega + \int_{\partial\Omega}\left(g_f l_c \mathbf{n}\cdot\nabla d\ \delta\dot{d}\right)\mathrm{d}\partial\Omega - \int_{\Omega}\frac{g_f}{l_c}\left(l_c^2\nabla^2 d\ \delta\dot{d} - d\delta\dot{d}\right)\mathrm{d}\Omega + \int_{\Omega}\omega\dot{d}\cdot\delta\dot{d}\ \mathrm{d}\Omega = 0. \tag{13}$$

The above equation is equivalent to,

$$\begin{aligned} &-\int_{\Omega}(1-d)\mathscr{H}(\mathbf{v},\bar{\varepsilon}^p)\delta\dot{d}\mathrm{d}\Omega + l_c^2\int_{\partial\Omega}\mathbf{n}\cdot\nabla d\delta\dot{d}\mathrm{d}\partial\Omega \\ &+\int_{\Omega}\left(-l_c^2\nabla d\cdot\nabla d\ + d\right)\delta\dot{d}\mathrm{d}\Omega + \frac{l_c}{g_f}\int_{\Omega}\omega\dot{d}\cdot\delta\dot{d}\mathrm{d}\Omega = 0. \end{aligned} \tag{14}$$

where $\mathscr{H}(\mathbf{u},\bar{\varepsilon}^p)$ stands for the crack driving force, which is non-decreasing during the loading process $0 \le s \le t$ to guarantee the irreversibility of damage, i.e.,

$$\mathscr{H}(\mathbf{u},\bar{\varepsilon}^p) := \underset{0\le s\le t}{max}(\mathscr{S}(\mathrm{state}(\mathbf{u},\bar{\varepsilon}^p))) \tag{15}$$

in which $\mathscr{S}(\mathrm{state}(\mathbf{u},\bar{\varepsilon}^p))$ denotes the crack driving state function and reads as:

$$\mathscr{S}(\mathrm{state}(\mathbf{u},\bar{\varepsilon}^p)) = \left\langle 2l_c \middle/ g_f\int_0^s (\mathbf{D}^e + \mathbf{D}^p) : \widetilde{\boldsymbol{\sigma}}\mathrm{d}s \right\rangle. \tag{16}$$

where $\langle\cdot\rangle := (\cdot + |\cdot|)/2$ is established by the Macaulay bracket.

The governing equation for plasticity can be derived as:

$$\int_{\Omega} -(1-d)^2\widetilde{\boldsymbol{\sigma}} : \delta\mathbf{D}^{\mathrm{p}}\mathrm{d}\Omega + \int_{\Omega}(1-d)^2\widetilde{\sigma}_y\delta\dot{\bar{\varepsilon}}^p\ \mathrm{d}\Omega = 0, \tag{17}$$

In line with Eq. (5), the above equation can be converted into:

$$\int_{\Omega}(1-d)^2\left(\widetilde{f}(\mathbf{u}) - \widetilde{\sigma}_y\right)\delta\dot{\bar{\varepsilon}}^p\mathrm{d}\Omega = 0 \tag{18}$$

2.1.3. Strong form

Based on Eq. (12), the governing equation for displacement field can be expressed as:

$$\mathrm{div}\ \boldsymbol{\sigma} + \mathbf{f} = \rho\ddot{\mathbf{u}} \text{ in } \Omega\times[0,t], \tag{19a}$$

$$\mathbf{n}\cdot\boldsymbol{\sigma} = \mathbf{t} \text{ on } \partial\Omega^s\times[0,t]. \tag{19b}$$

Along with the Dirichlet boundary condition

$$\mathbf{u} = \widetilde{\mathbf{u}} \text{ on } \partial\Omega^{\mathrm{h}}\times[0,t]. \tag{19c}$$

The governing equation for phase field is derived as,

$$\varpi \dot{d} = (1-d)\mathscr{H}(\mathbf{u}, \bar{\varepsilon}^p) - \left(d - l_c^2 \nabla d \cdot \nabla d\right), \quad \text{in } \Omega \times [0,t], \tag{20}$$

$$\mathbf{n} \cdot \nabla d = 0, \ \text{in } \partial\Omega \times [0,t]. \tag{21}$$

where $\varpi = \omega l_c / g_f$ is a modified viscosity parameter which is consistent with our previous work (Li et al., 2023, Li et al., 2022a).

Concerning the plasticity, the plastic governing equation in a strong form can be expressed from Eq. (18) as,

$$F^p(\mathbf{u}, \bar{\varepsilon}^p, \dot{\bar{\varepsilon}}^p, T) = \widetilde{f}(\widetilde{\boldsymbol{\sigma}}) - \widetilde{\sigma}_y(\bar{\varepsilon}^p, \dot{\bar{\varepsilon}}^p, T) = 0, \tag{22}$$

where $\widetilde{\sigma}_y$ denotes undamaged flow stress, which is dependent on equivalent plastic strain, strain rate, and temperature.

According to Eq. (5) as well as the Euler's identity, i.e., $\widetilde{f}(\mathbf{u}) = \widetilde{\sigma} : \frac{\partial \widetilde{f}(\mathbf{u})}{\partial \boldsymbol{\sigma}}$, the associated flow rule can be derived as:

$$\frac{\mathbf{D}^p}{\dot{\bar{\varepsilon}}^p} = \frac{\mathrm{d}\widetilde{f}(\widetilde{\boldsymbol{\sigma}})}{\mathrm{d}\widetilde{\boldsymbol{\sigma}}} = \frac{\partial f(\boldsymbol{\sigma}, d)}{\partial \boldsymbol{\sigma}} = \mathbf{a} \ \Rightarrow \mathbf{D}^p = \dot{\bar{\varepsilon}}^p \mathbf{a}. \tag{23}$$

Note that Eq. (22) holds in the case of plastic loading and neutral loading. Specially, they meet the following conditions:

Plastic loading: $F^p = 0$ and $\dot{\bar{\varepsilon}}^p > 0$;

Neutral loading: $F^p = 0$ and $\dot{\bar{\varepsilon}}^p = 0$.

Together with elastic loading and unloading: $F^p < 0$ and $\dot{\bar{\varepsilon}}^p = 0$, the complete Karush-Kuhn-Tucker (KKT) complementarity conditions read as follows (Simo and Hughes, 2006):

$$F^p \le 0, \ F^p \dot{\bar{\varepsilon}}^p = 0, \ \dot{\bar{\varepsilon}}^p \ge 0. \tag{24}$$

2.2. Thermal evolution

In dynamic loading, temperature would change due to heat generation from mechanical work during the loading process (Luscher et al., 2018). In this study, the temperature is treated as an internal state variable that can be determined via (Roth and Mohr, 2014),

$$dT = \varsigma(\dot{\bar{\varepsilon}}^p) \frac{\chi}{\rho C_p} \widetilde{\sigma}_y d\bar{\varepsilon}^p, \tag{25}$$

in which Taylor–Quinney coefficient χ quantifies the fraction of plastic work converted to heat, ρ denotes the mass density, and C_p represents the heat capacity. The strain rate-dependent factor ς exhibits variation within a range of 0 to 1. The limiting values of $\varsigma = 0$ and $\varsigma = 1$ correspond to isothermal and adiabatic conditions, respectively. Under a low strain rate, diffusion tends to occur significantly faster than the rate of heat generation, leading to isothermal conditions ($\varsigma = 0$). Conversely, at a high strain rate, diffusion occurs much slower than the rate of heat generation, resulting in adiabatic conditions ($\varsigma = 1$). The temperature increase for intermediate strain rates is approximated in an *ad hoc* manner through the parametric form (Roth and Mohr, 2014):

$$\varsigma(\dot{\bar{\varepsilon}}_p) = \begin{cases} 0, & \dot{\bar{\varepsilon}}^p < \dot{\varepsilon}_{it}, \\ \dfrac{\left(\dot{\bar{\varepsilon}}_p - \dot{\varepsilon}_{it}\right)^2 \left(3\dot{\varepsilon}_a - 2\dot{\bar{\varepsilon}}_p - \dot{\varepsilon}_{it}\right)}{\left(\dot{\varepsilon}_a - \dot{\varepsilon}_{it}\right)^3}, & \dot{\varepsilon}_{it} \leqslant \dot{\bar{\varepsilon}}^p \leqslant \dot{\varepsilon}_a, \\ 1, & \dot{\bar{\varepsilon}}^p > \dot{\varepsilon}_a, \end{cases} \tag{26}$$

where the parameters $\dot{\varepsilon}_{it}$ and $\dot{\varepsilon}_a$ define the critical strain rates for the isothermal and adiabatic conditions, respectively. For simplicity, the reference strain rate $\dot{\varepsilon}_0$ in the modified Johnson-Cook model (see Section 3.1.2) is treated as the isothermal limit, i.e. $\dot{\varepsilon}_{it} = \dot{\varepsilon}_0$ (Roth and Mohr, 2014).

In addition to the proportion of plastic work converted into heat, the remaining proportion contributes to driving the phase-field cracking process. Thus, the crack driving state function should be modified as

$$\mathscr{S}(\text{state}(\mathbf{u}, \bar{\varepsilon}^p)) = 2l_c \Big/ g_f \int_0^s [\widetilde{\boldsymbol{\sigma}} : \mathbf{D}^e + (1 - \varsigma\chi)\widetilde{\boldsymbol{\sigma}} : \mathbf{D}^p] \mathrm{d}s. \tag{27}$$

3. Hypoelastic-plasticity and fracture criteria

The orientation, strain rate, and stress state dependent constitutive relations are derived for general metallic materials. The crack driving force for the phase field model is derived accordingly.

3.1. Rate dependent anisotropic plasticity model

3.1.1. Hill48 plasticity model

Orientation dependent plastic behaviour presents commonly in conventional sheet metals (Banabic, 2010) and laser powder bed fusion (LPBF) printed metallic materials (Carroll et al., 2015). To describe this phenomenon, a classical Hill48 plasticity model (Hill, 1948) is employed in this study. The equivalent stress $\widetilde{f}(\widetilde{\sigma})$ is defined as:

$$\widetilde{f}(\widetilde{\boldsymbol{\sigma}}) = \sqrt{\begin{array}{c} F\left(\widetilde{\sigma}_{yy}-\widetilde{\sigma}_{zz}\right)^2 + G\left(\widetilde{\sigma}_{zz}-\widetilde{\sigma}_{xx}\right)^2 + H\left(\widetilde{\sigma}_{zz}-\widetilde{\sigma}_{yy}\right)^2 \\ +2L\widetilde{\sigma}_{yz}^2 + 2M\widetilde{\sigma}_{zx}^2 + 2N\widetilde{\sigma}_{xy}^2 \end{array}}, \tag{28}$$

where $F, G, H, L, M,$ and N denote the anisotropic parameters, $\widetilde{\sigma}_{xx}$, $\widetilde{\sigma}_{yy}$, and $\widetilde{\sigma}_{zz}$ are the normal stresses, and $\widetilde{\sigma}_{xy}$, $\widetilde{\sigma}_{yz}$, $\widetilde{\sigma}_{zx}$ represent the shear stress components. Note that Hill48 function can be extended to be pressure dependent for pressure sensitive metals (Caddell et al., 1973; Deshpande et al., 2001). In this study, the printing plane is assumed to be xz plane and y-axis refers to building direction. Correspondingly, the work conjugated equivalent plastic strain rate $\dot{\bar{\varepsilon}}^p$ reads as,

$$\dot{\bar{\varepsilon}}^p = \sqrt{\frac{F\left(\dot{\varepsilon}_{xx}^p\right)^2 + G\left(\dot{\varepsilon}_{yy}^p\right)^2 + H\left(\dot{\varepsilon}_{zz}^p\right)^2}{FG+FH+GH} + \frac{2\left(\dot{\varepsilon}_{xy}^p\right)^2}{L} + \frac{2\left(\dot{\varepsilon}_{xz}^p\right)^2}{M} + \frac{2\left(\dot{\varepsilon}_{yz}^p\right)^2}{N}}, \tag{29}$$

where $\dot{\varepsilon}_{xx}^p$, $\dot{\varepsilon}_{yy}^p$, $\dot{\varepsilon}_{zz}^p$, $\dot{\varepsilon}_{xy}^p$, $\dot{\varepsilon}_{xz}^p$, and $\dot{\varepsilon}_{yz}^p$ are components of plastic strain rate.

3.1.2. Modified Johnson-Cook model

To consider the influence of strain rate hardening and thermal softening, the flow stress is expressed as:

$$\widetilde{\sigma}_y(\bar{\varepsilon}^p, \dot{\bar{\varepsilon}}^p, T) = \widetilde{\sigma}_0(\bar{\varepsilon}^p)\left[1 + C_0 \mathrm{e}^{C_1\bar{\varepsilon}^p} \ln\left(\frac{\dot{\bar{\varepsilon}}^p}{\dot{\varepsilon}_0}\right)\right](1-\widehat{T}^m), \tag{30}$$

where $\widetilde{\sigma}_0(\bar{\varepsilon}^p)$ can be described by combination of the Swift and Voce function (Pack et al., 2014) or piecewise linear functions (Li et al., 2022a) to achieve satisfactory predicting accuracy in the quasi-static loading condition; $\dot{\varepsilon}_0$ denotes the reference strain rate; C_0, C_1, and $\dot{\varepsilon}_0$ are used to describe strain rate dependency. Compared with the classical Johnson-Cook model, it is noted that $C_0\mathrm{e}^{C_1\bar{\varepsilon}^p}$ is dependent on $\bar{\varepsilon}^p$ rather than a constant, which showed better predicting accuracy; and a similar approach can be found in (Li et al., 2022b; Tang et al., 2021). m is a material parameter and $\widehat{T}$ is a factor to consider thermal softening and defined as,

$$\widehat{T} = \begin{cases} 0, & T < T_{room}\ , \\ \dfrac{(T - T_{room})}{(T_{melt} - T_{room})}, & T_{room} \le T \le T_{melt}\ , \\ 1, & T > T_{melt}\ . \end{cases} \tag{31}$$

where T, T_{room} and T_{melt} are current, room and melting temperature, respectively.

3.2. Ductile fracture criteria

Ductile fracture is highly dependent on stress states, characterised by stress triaxiality η and Lode angle parameter $\overline{\theta}$ (Bai and Wierzbicki, 2008; Lou et al., 2014). Ductile fracture is highly dependent on stress states, characterised by stress triaxiality η and Lode angle parameter $\overline{\theta}$ (Bai and Wierzbicki, 2008; Lou et al., 2014). Firstly, the relationship between the principal stresses $\widetilde{\sigma}_1$, $\widetilde{\sigma}_2$ and $\widetilde{\sigma}_3$, and the invariants p, r and q of the stress tensor are given as:

$$p = -\frac{1}{3}\mathrm{tr}\widetilde{\sigma} = -\frac{1}{3}(\widetilde{\sigma}_1 + \widetilde{\sigma}_2 + \widetilde{\sigma}_3), \tag{32}$$

$$r = \sqrt{\frac{1}{2}[(\widetilde{\sigma}_1 - \widetilde{\sigma}_2)^2 + (\widetilde{\sigma}_2 - \widetilde{\sigma}_3)^2 + (\widetilde{\sigma}_3 - \widetilde{\sigma}_1)^2]}, \tag{33}$$

$$q = \left[\frac{27}{2}(\widetilde{\sigma}_1 + p)(\widetilde{\sigma}_2 + p)(\widetilde{\sigma}_3 + p)\right]^{\frac{1}{3}}. \tag{34}$$

Then, the stress triaxiality η and Lode angle parameter $\overline{\theta}$ are defined as:

$$\eta = -\frac{p}{r}, \tag{35}$$

$$\overline{\theta} = 1 - \frac{2}{\pi}\arccos\left(\frac{q}{r}\right)^3. \tag{36}$$

According to the value of stress triaxiality, high stress triaxiality ($\eta > 2/3$), medium stress triaxiality ($1/3 < \eta < 2/3$) tension, tension-shear ($1/10 < \eta < 1/3$), shear ($-1/10 < \eta < 1/10$), and compression-shear ($-1/3 < \eta < -1/10$) also frequently used in the literature (Jackiewicz, 2011; Kang et al., 2016; Peng et al., 2021). For metallic materials, a cut-off region ($\eta < -1/3$) is commonly employed to control non-physical compressive damage (Bao and Wierzbicki, 2004; Lou et al., 2014).

The Modified Mohr-Coulomb (MMC) model is considered in this study to be combined with the presented phase field model as it demonstrates the ability to predict crack initiation and direction with good accuracy (Bai and Wierzbicki, 2009). It transforms the classical Mohr-Coulomb criterion from a shear stress and normal stress representation to a mixed strain-stress representation $(\overline{\varepsilon}^f, \eta, \overline{\theta})$. The fracture strain is defined as:

$$\overline{\varepsilon}^f(\eta, \overline{\theta}, \dot{\overline{\varepsilon}}^p) = b\left\{\frac{A}{c_2}\left[c_3 + \frac{\sqrt{3}}{2-\sqrt{3}}(1-c_3)\left(\sec\left(\frac{\overline{\theta}\pi}{6}\right) - 1\right)\right]\left[\sqrt{\frac{1+c_1^2}{3}}\cos\left(\frac{\overline{\theta}\pi}{6}\right) + c_1\left(\eta + \frac{1}{3}\sin\left(\frac{\overline{\theta}\pi}{6}\right)\right)\right]\right\}^{-\frac{1}{n}}, \tag{37}$$

where b is used to describe the strain rate effect on the fracture strain. Based on experimental data in our previous study (Liu et al., 2024), b is defined as,

$$b = \begin{cases} 1, & \dot{\overline{\varepsilon}}^p < \dot{\varepsilon}_0 \\ \max\left(\mathrm{b}_0,\ 1 - \gamma \mathrm{In}(\dot{\overline{\varepsilon}}^{\mathrm{p}}/\dot{\varepsilon}_0)\right), & \dot{\overline{\varepsilon}}^p \geq \dot{\varepsilon}_0. \end{cases} \tag{38}$$

In real-life practice, the loadings are commonly non-proportional, i.e., η and $\overline{\theta}$ vary during the loading history. Thus, it would be indispensable to introduce a loading history dependent damage indicator D defined as (Bai and Wierzbicki, 2009):

$$D(\overline{\varepsilon}^p) = \int_0^{\overline{\varepsilon}^p} \frac{\mathrm{d}\overline{\varepsilon}^p}{\overline{\varepsilon}^f(\eta, \overline{\theta})}. \tag{39}$$

Damage is assumed to initiate when $D = 1$.

Similar to plastic behaviour, laser powder bed fusion (LPBF) printed metallic materials also exhibit orientation-dependent fracture (Wilson-Heid et al., 2020). To capture such phenomena, an anisotropic fracture model is adopted in terms of a linear transformation of the plastic strain tensor (Luo et al., 2012) in this work. In a vector notation, the equivalent plastic strain can be modified to account anisotropy as:

$$\dot{\overline{\varepsilon}}^{p,\ ani} = \sqrt{\frac{2}{3}[\boldsymbol{\beta}\cdot(\dot{\boldsymbol{\varepsilon}}^p)]^{\mathrm{T}}\cdot[\boldsymbol{\beta}\cdot(\dot{\boldsymbol{\varepsilon}}^p)]}, \tag{40}$$

where $\dot{\boldsymbol{\varepsilon}}^p = \left[\dot{\varepsilon}^p_{xx}, \dot{\varepsilon}^p_{yy}, \dot{\varepsilon}^p_{zz}, \sqrt{2}\,\dot{\varepsilon}^p_{xy}, \sqrt{2}\,\dot{\varepsilon}^p_{yz}, \sqrt{2}\,\dot{\varepsilon}^p_{zx}\right]^{\mathrm{T}}$ is the plastic strain rate. $\boldsymbol{\beta}$ characterises the linear transformation defined as:

$$\boldsymbol{\beta} = \begin{bmatrix} \beta_{xx} & 0 & 0 & 0 & 0 & 0 \\ 0 & \beta_{yy} & 0 & 0 & 0 & 0 \\ 0 & 0 & \beta_{zz} & 0 & 0 & 0 \\ 0 & 0 & 0 & \beta_{xy} & 0 & 0 \\ 0 & 0 & 0 & 0 & \beta_{yz} & 0 \\ 0 & 0 & 0 & 0 & 0 & \beta_{zx} \end{bmatrix} \tag{41}$$

3.3. Stress-state, rate, and orientation dependent crack driving force

To better match the experimental observation that damage initiates after a certain level of deformation, Miehe et al. (2015) proposed an energy-based and strain-based damage threshold. Following this concept, various damage thresholds have been used, e.g. energy-based threshold in (Dean et al., 2020; Dittmann et al., 2020) and strain-based threshold in (Alessi et al., 2018; Noii et al., 2021). Nevertheless, the abovementioned damage thresholds are taken as constants; and the threshold should be stress state, strain rate and orientation dependent (Abrari Vajari et al., 2022; Li et al., 2022a). An energy based threshold is defined as (Li et al., 2023, Li et al., 2022a):

$$\widetilde{\varphi}_{cr} = \int_0^s (\mathbf{D}^e + (1-\varsigma\chi)\mathbf{D}^p) : \widetilde{\boldsymbol{\sigma}}\mathrm{d}s|_{D=1}. \tag{42}$$

Accordingly, the crack driving state function is revisited as

$$\mathscr{S}(\mathrm{state}(\mathbf{u}, \overline{\varepsilon}^p)\ ) = 2l_c \Big/ g_f\widetilde{\varphi}_{cr}\left\langle \int_0^s (\mathbf{D}^e + (1-\varsigma\chi)\mathbf{D}^p) : \widetilde{\boldsymbol{\sigma}}\mathrm{d}s \Big/ \widetilde{\varphi}_{cr} - 1 \right\rangle. \tag{43}$$

4. Finite element implementation

This section introduces spatial and temporal discretisation for the proposed model. The cutting-plane algorithm will also be introduced within hypoelastic-viscoplastic constitutive relations for plastic calculation. For convenience, matrix/vector notation is used in this section.

4.1. Spatial discretisation

The proposed model is numerically implemented in the finite element framework based upon the weak form defined in Eqs. (11) and (14) together with the constitutive equations, Eqs. (28), (31) and (37). A mixed finite element formulation for displacement field $\mathbf{u}$ and phase field d is implemented here, whose spatial discretisation is considered as follows:

$$\mathbf{u}^e = \sum_{I=1}^{N_n} N^e_{\mathbf{u}I}\mathbf{u}^e_I,\ d^e = \sum_{I=1}^{N_n} N^e_{dI}d^e_I, \tag{44}$$

$$\dot{\mathbf{u}}^e = \sum_{I=1}^{N_n} N^e_{\mathbf{u}I}\dot{\mathbf{u}}^e_I, \ddot{\mathbf{u}}^e = \sum_{I=1}^{N_n} N^e_{\mathbf{u}I}\ddot{\mathbf{u}}^e_I, \dot{d}^e = \sum_{I=1}^{N_n} N^e_{dI}\dot{d}^e_I. \tag{45}$$

where $N^e_{\mathbf{u}I}$ and N^e_{dI} stand for the shape functions associated with node I, and $\mathbf{u}^e_I$ and d^e_I are the nodal displacement-field and phase-field at node I of element e, respectively. N_n is the number of nodes in element e.

The velocity gradient and phase field gradient are given by:

$$\mathbf{L}^e = \sum_{I=1}^{N_n} \mathbf{B}^e_{\mathbf{u}I}\dot{\mathbf{u}}^e_I, \nabla d^e = \sum_{I=1}^{N_n} \mathbf{B}^e_{dI}\dot{d}^e_I, \tag{46}$$

where $\mathbf{B}^e_{\mathbf{u}I}$ is the matrix with spatial derivatives of $N^e_{\mathbf{u}I}$ with respect to the current configuration and $\mathbf{B}^e_{dI}$ is the matrix with spatial derivatives of N^e_{dI} with respect to the reference configuration.

The test functions and their derivatives are discretised as:

$$\delta\dot{\mathbf{u}}^e = \sum_{I=1}^{N_n} N^e_{\mathbf{u}I}\delta\dot{\mathbf{u}}^e_I, \quad \delta\dot{d}^e = \sum_{I=1}^{N_n} N^e_{dI}\delta\dot{d}^e_I \tag{47}$$

$$\delta\mathbf{L}^e = \sum_{I=1}^{N_n} \mathbf{B}^e_{\mathbf{u}I}\delta\dot{\mathbf{u}}^e_I, \delta\nabla\dot{d}^e = \sum_{I=1}^{N_n} \mathbf{B}^e_{dI}\delta\dot{d}^e_I. \tag{48}$$

After assembling the elements in the global system, the spatially discretised equation of the displacement problem is obtained as:

$$\mathbf{M}\ddot{\mathbf{u}} = \mathbf{F}^{\text{ext}} - \mathbf{F}^{\text{int}}, \tag{49}$$

where $\mathbf{u} = \{\mathbf{u}^e\}$ represents the displacement vector containing all the nodal values of the solution domain. $\mathbf{M}$, $\mathbf{F}^{\text{ext}}$, and $\mathbf{F}^{\text{int}}$ are the mass matrix, externally applied load vector and internal force vector, respectively, expressed as follows:

$$\mathbf{M} = \wedge_{N_e}^{e=1}\int_\Omega \rho\mathbf{N}^{e\,\mathrm{T}}_{\mathbf{u}}\mathbf{N}^e_{\mathbf{u}}\mathrm{d}\Omega, \tag{50}$$

$$\mathbf{F}^{\text{int}} = \wedge_{N_e}^{e=1}\int_\Omega \mathbf{B}^{e\,\mathrm{T}}_{\mathbf{u}}\boldsymbol{\sigma}\mathrm{d}\Omega, \tag{51}$$

$$\mathbf{F}^{\text{ext}} = \wedge_{N_e}^{e=1}\left(\int_\Omega \mathbf{N}^{e\,\mathrm{T}}_{\mathbf{u}}\mathbf{b}\mathrm{d}\Omega + \int_{\partial\Omega^s}\mathbf{N}^{e\,\mathrm{T}}_{\mathbf{u}}\mathbf{t}\mathrm{d}\partial\Omega^s\right), \tag{52}$$

where the operator $\wedge_{N_e}^{e=1}$ represents the element to global assembly in the finite element formulation with N_e being the number of elements in the solution domain.

Similarly, the spatially discretised equation of the phase field problem reads:

$$\mathbf{C}\dot{\mathbf{d}} = \mathbf{Y}, \tag{53}$$

with

$$\mathbf{C} = \wedge_{N_e}^{e=1} \int_{\Omega} \varpi \mathbf{N}_d^{e\mathrm{T}} \mathbf{N}_d^e \mathrm{d}\Omega, \tag{54}$$

$$\mathbf{Y} = -\wedge_{N_e}^{e=1} \int_{\Omega} \left\{ [d - 2(1-d)\mathscr{H}] \mathbf{N}_d^{e\mathrm{T}} + l_c^2 \mathbf{B}_d^{e\mathrm{T}} \nabla d \right\} \mathrm{d}\Omega, \tag{55}$$

where $\mathbf{d} = \{d^e\}$ stands for the phase field vector containing all the nodal values in the solution domain.

4.2. Temporal discretisation

The equations will be solved using the explicit time integration schemes for both the displacement field and phase field. We consider a finite time increment $[t_n, t_{n+1}]$, and $\Delta t_{n+1} = t_{n+1} - t_n$ denotes the current increment size. The time integration of the displacement field is performed by the central difference method:

$$\ddot{\mathbf{u}}_n = \mathbf{M}^{-1} \left(\mathbf{F}^{\mathrm{ext}} - \mathbf{F}^{\mathrm{int}} \right), \tag{56}$$

$$\dot{\mathbf{u}}_{n+\frac{1}{2}} = \dot{\mathbf{u}}_{n-\frac{1}{2}} + \frac{\Delta t_n + \Delta t_{n+1}}{2} \ddot{\mathbf{u}}_n, \tag{57}$$

$$\mathbf{u}_{n+1} = \mathbf{u}_n + \Delta t_{n+1} \, \dot{\mathbf{u}}_{n+\frac{1}{2}}, \tag{58}$$

where the subscript n refers to the increment number and $\left(n - \frac{1}{2}\right)$ and $\left(n + \frac{1}{2}\right)$ refers to the mid-increment values. Given that the variables $\ddot{\mathbf{u}}_n$, $\dot{\mathbf{u}}_{n-\frac{1}{2}}$ and $\mathbf{u}_n$ have been known from the previous increment, $\mathbf{u}_{n+1}$ can be computed using the explicit time integration method. Note that a special treatment is required for the initial conditions of velocity as:

$$\dot{\mathbf{u}}_{+\frac{1}{2}} = \dot{\mathbf{u}}_0 + \frac{\Delta t_1}{2} \ddot{\mathbf{u}}_0, \tag{59}$$

$$\dot{\mathbf{u}}_{-\frac{1}{2}} = \dot{\mathbf{u}}_0 - \frac{\Delta t_1}{2} \ddot{\mathbf{u}}_0. \tag{60}$$

The time integration of the phase field is performed by the forward finite difference method:

$$\dot{\mathbf{d}}_n = \mathbf{C}^{-1} \mathbf{Y}, \tag{61}$$

$$\mathbf{d}_{n+1} = \mathbf{d}_n + \Delta t_{n+1} \dot{\mathbf{d}}_n. \tag{62}$$

In order to improve computational efficiency for the explicit time integration schemes, the lumped or diagonal matrices $\mathbf{M}$ and $\mathbf{C}$ are used (Belytschko et al., 2014) and determined at the beginning of each increment. The commonly used row-sum technique is used in this study, the diagonal matrices are determined by (Belytschko et al., 2014):

$$\mathbf{M}_{II}^D = \sum_J M_{IJ}, \tag{63}$$

$$\mathbf{C}_{II}^D = \sum_J C_{IJ}. \tag{64}$$

4.3. Incrementally objective integration of hypoelastic-plastic constitutive equations

The algorithmic implementation of the hypoelastic-based plasticity model requires to use an incrementally objective integration algorithm (Hughes and Winget, 1980) to maintain the frame-indifference of the formulation. The rate dependent constitutive equations are transformed to a local configuration that is unaffected by superposed spatial rigid body motions. Then a time integration algorithm is performed in this local configuration, and finally, the discrete equations are transformed back to the spatial configuration.

4.3.1. Corotational formulation

The formulation herein employs a corotational local coordinate system for a rotational neutralised description of the constitutive equations of hypoelastic-plasticity (Simo and Hughes, 2006). The rate of deformation tensor $\mathbf{D}$ is assumed to be additively decomposed into an elastic component $\mathbf{D}^{\mathrm{e}}$ and a plastic component $\mathbf{D}^{\mathrm{p}}$ as:

$$\mathbf{D} = \mathbf{D}^e + \mathbf{D}^{\mathrm{p}}. \tag{65}$$

Eq. (65) is sometimes considered to be an *ad hoc* finite strain extension of the additive decomposition of the strain tensor in the infinitesimal elastoplastic theory (Brepols et al., 2014). However, hypoelastic-plasticity does not deviate noticeably from the

hyperelastic-plasticity counterpart, especially in the application of metallic plasticity (Brepols et al., 2014). The hypoelastic response of the material is expressed in terms of a linear relationship between an objective rate of the Kirchhoff stress $\overset{\nabla}{\boldsymbol{\tau}}$ and $\mathbf{D}^{\mathrm{e}}$ as:

$$\overset{\nabla}{\boldsymbol{\tau}} = \mathbf{E}\mathbf{D}^{\mathrm{e}} = \mathbf{E}(\mathbf{D} - \mathbf{D}^{\mathrm{p}}). \tag{66}$$

Note that for the material whose plastic flow is approximately isochoric (volume preserving) and elastic strains are small, the Kirchhoff stress $\overset{\nabla}{\boldsymbol{\tau}}$ and Cauchy stress $\overset{\nabla}{\boldsymbol{\sigma}}$ are approximately the same (Brepols et al., 2014). This is the case in the presented Hill48 plastic theory, leading to $\boldsymbol{\tau} \approx \boldsymbol{\sigma}$. Combining with standard hypoelastic-plasticity formulation based on the Kirchhoff stress and the Jaumann rate (Simo and Hughes, 2006), the following equation can be derived:

$$\overset{\nabla}{\boldsymbol{\sigma}} \approx \overset{\nabla}{\boldsymbol{\tau}} = \dot{\boldsymbol{\sigma}} - \boldsymbol{\Omega}\boldsymbol{\sigma} + \boldsymbol{\sigma}\boldsymbol{\Omega}, \tag{67}$$

in which $\boldsymbol{\Omega}$ is a skew-symmetric second-order tensor or spin tensor which satisfies $\boldsymbol{\Omega}^{\mathrm{T}} = -\boldsymbol{\Omega}$ (Kim, 2014).

An incrementally objective update formulation for hypoelastic constitutive relation in Eq. (66) is presented here. The coordinate system is attached at each point in the body and then rotates with the material during deformation. The following initial value problem shall be addressed for the proper orthogonal rotation tensor $\boldsymbol{\Lambda}$:

$$\dot{\boldsymbol{\Lambda}} = \boldsymbol{\Omega}\boldsymbol{\Lambda} \text{ with } \boldsymbol{\Lambda}|_{t=0} = \mathbf{I}. \tag{68}$$

This implies that it is possible to transform the tensorial quantities from the spatial description to the corotational description by pre-multiplying and post-multiplying them with $\boldsymbol{\Lambda}^{\mathrm{T}}$ and $\boldsymbol{\Lambda}$, respectively. The corotational Cauchy stress $\widehat{\widetilde{\boldsymbol{\sigma}}}$, corotational rate of deformation $\widehat{\mathbf{D}}$, and plastic part of the corotational rate of deformation $\widehat{\mathbf{D}}^{\mathrm{p}}$ are given as follows:

$$\widehat{\widetilde{\boldsymbol{\sigma}}} = \boldsymbol{\Lambda}^{\mathrm{T}}\,\widetilde{\boldsymbol{\sigma}}\boldsymbol{\Lambda},\ \widehat{\mathbf{D}} = \boldsymbol{\Lambda}^{\mathrm{T}}\boldsymbol{D}\boldsymbol{\Lambda},\ \widehat{\mathbf{D}}^{\mathrm{p}} = \boldsymbol{\Lambda}^{\mathrm{T}}\mathbf{D}^{\mathrm{p}}\boldsymbol{\Lambda}. \tag{69}$$

Differentiating the first equation in Eq. (69) with respect to time leads to

$$\dot{\widehat{\widetilde{\boldsymbol{\sigma}}}} = \boldsymbol{\Lambda}^{\mathrm{T}}(\,\dot{\widetilde{\boldsymbol{\sigma}}} - \boldsymbol{\Omega}\widetilde{\boldsymbol{\sigma}} + \widetilde{\boldsymbol{\sigma}}\boldsymbol{\Omega})\boldsymbol{\Lambda} = \boldsymbol{\Lambda}^{\mathrm{T}}\overset{\nabla}{\widetilde{\boldsymbol{\sigma}}}\boldsymbol{\Lambda}. \tag{70}$$

Due to the isotropy of $\mathbf{E}$ (i.e., $\mathbf{E}= \widehat{\mathbf{E}}$), the hypoelastic relation in Eq. (66) may be transformed to a rotation-neutralised form as:

$$\dot{\widehat{\widetilde{\boldsymbol{\sigma}}}} = \mathbf{E}(\widehat{\mathbf{D}} - \widehat{\mathbf{D}}^{\mathrm{p}}). \tag{71}$$

Using the approximations proposed in the Hughes-Winget algorithm (Hughes and Winget, 1980) and applying the generalised midpoint rule to Eq. (71), the following update formula can be derived for the corotational Cauchy stress:

$$\widehat{\widetilde{\boldsymbol{\sigma}}}_{n+1} = \widehat{\widetilde{\boldsymbol{\sigma}}}_{n} + \Delta t_{n+1}\boldsymbol{\Lambda}_{\mathbf{n+1}}^{\mathbf{T}}\dot{\widehat{\widetilde{\boldsymbol{\sigma}}}}\boldsymbol{\Lambda}_{n+1} = \widehat{\widetilde{\boldsymbol{\sigma}}}_{n} + \Delta t_{n+1}\mathbf{E}\big(\widehat{\mathbf{D}}_{n+\alpha} - \widehat{\mathbf{D}}^{\mathrm{p}}_{n+\alpha}\big),\ 0 \le \alpha \le 1. \tag{72}$$

A specific value for α leads to a specific integration algorithm, e.g., $\alpha = 0$ for explicit Euler, $\alpha = 1/2$ for the mid-point rule, and $\alpha = 1$ for implicit Euler. Then, the equation must be mapped back to the spatial description by pre- and post-multiplying them with $\boldsymbol{\Lambda}$ and $\boldsymbol{\Lambda}^{\mathrm{T}}$, respectively, given as,

$$\widetilde{\boldsymbol{\sigma}}_{n+1} = \boldsymbol{\Lambda}_{\Delta}\,\widetilde{\boldsymbol{\sigma}}_{n}\boldsymbol{\Lambda}_{\Delta}^{\mathrm{T}} + \Delta t_{n+1}\boldsymbol{E}\boldsymbol{\Lambda}_{\delta}\big(\mathbf{D}_{n+\alpha} - \mathbf{D}^{\mathrm{p}}_{n+\alpha}\big)\boldsymbol{\Lambda}_{\delta}^{\mathrm{T}}. \tag{73}$$

where $\boldsymbol{\Lambda}_{\Delta}$ is the incremental rotation tensor between t_n and t_{n+1}, and $\boldsymbol{\Lambda}_{\delta}$ between t_n and $t_{n+\alpha}$:

$$\boldsymbol{\Lambda}_{\Delta} := \boldsymbol{\Lambda}_{n+1}\boldsymbol{\Lambda}_{n}^{\mathrm{T}},\quad \boldsymbol{\Lambda}_{\delta} := \boldsymbol{\Lambda}_{n+1}\boldsymbol{\Lambda}_{n+\alpha}^{\mathrm{T}}. \tag{74}$$

in which the rotation tensors $\boldsymbol{\Lambda}_{n+1}$, $\boldsymbol{\Lambda}_{n+\alpha}$ and $\boldsymbol{\Lambda}_{n}$ are obtained according to the particular choice of rotational stress rate (Simo and Hughes, 2006).

In this study, the Green-Naghdi rate-based plasticity model is used, i.e., the skew-symmetric tensor $\boldsymbol{\Omega} = \dot{\mathbf{R}}\mathbf{R}^{\mathrm{T}}$ in Eq. (68) with $\mathbf{R}$ being the rotation tensor resulting from the polar decomposition of the deformation gradient. Then, the exact solution to problem (68) is give as,

$$\boldsymbol{\Lambda} = \mathbf{R}. \tag{75}$$

As a result, $\boldsymbol{\Lambda}_{\Delta}$ and $\boldsymbol{\Lambda}_{\delta}$ are redefined as,

$$\boldsymbol{\Lambda}_{\Delta} = \mathbf{R}_{\Delta} = \mathbf{R}_{n+1}\mathbf{R}_{n}^{\mathrm{T}},\ \boldsymbol{\Lambda}_{\delta} = \mathbf{R}_{\delta} = \mathbf{R}_{n+1}\mathbf{R}_{n+\alpha}^{\mathrm{T}}. \tag{76}$$

in which the rotations $\mathbf{R}_{n+1}$, $\mathbf{R}_{n}$ and $\mathbf{R}_{n+\alpha}$ are obtained, respectively from the polar decomposition of the deformation gradients $\mathbf{F}_{n+1}$, $\mathbf{F}_{n}$ and $\mathbf{F}_{n+\alpha}$.

Using the flow rule defined in Eq. (23), i.e., $\mathbf{D}^{\mathrm{p}} = \dot{\bar{\varepsilon}}^{p}\mathbf{a}$, Eq. (73) can be rewritten as:

$$\widetilde{\boldsymbol{\sigma}}_{n+1} = \widetilde{\boldsymbol{\sigma}}_{n+1}^{\mathrm{trial}} - \Delta\bar{\varepsilon}^{p}\boldsymbol{E}\boldsymbol{\Lambda}_{\delta}\mathbf{a}_{n+\alpha}\boldsymbol{\Lambda}_{\delta}^{\mathrm{T}}, \tag{77}$$

where $\Delta\bar{\varepsilon}^p = \Delta t_{n+1}\dot{\bar{\varepsilon}}^p$; and $\boldsymbol{\sigma}_{n+1}^{\text{trial}}$ is the trial stress defined as,

$$\widetilde{\boldsymbol{\sigma}}_{n+1}^{\text{trial}} = \boldsymbol{\Lambda}_\Delta\, \widetilde{\boldsymbol{\sigma}}_n \boldsymbol{\Lambda}_\Delta^{\mathrm{T}} + \Delta t_{n+1}\mathbf{E}\boldsymbol{\Lambda}_\delta \mathbf{D}_{n+\alpha}\boldsymbol{\Lambda}_\delta^{\mathrm{T}}. \tag{78}$$

Eq. (72) suggests a two-step elastic predictor/plastic corrector. If the mid-point rule is applied for the elastic predictor and the material response of the stress increment is neglected ($\boldsymbol{\Lambda}_\delta \cong \mathbf{I}$), then the trial stress can be written as:

$$\widetilde{\boldsymbol{\sigma}}_{n+1}^{\text{trial}} = \boldsymbol{\Lambda}_\Delta\, \widetilde{\boldsymbol{\sigma}}_n \boldsymbol{\Lambda}_\Delta^{\mathrm{T}} + \Delta t_{n+1}\mathbf{E}\mathbf{D}_{n+\frac{1}{2}} = \boldsymbol{\Lambda}_\Delta\, \widetilde{\boldsymbol{\sigma}}_n \boldsymbol{\Lambda}_\Delta^{\mathrm{T}} + \mathbf{E}\Delta\mathbf{D} \tag{79}$$

in which the strain increment tensor $\Delta\mathbf{D}$ can be computed as

$$\Delta\mathbf{D} = \Delta t_{n+1}\mathbf{D}_{n+\frac{1}{2}} = \frac{1}{2}\left[\left(\frac{\partial\Delta\mathbf{u}}{\partial\mathbf{x}_{n+\frac{1}{2}}}\right) + \left(\frac{\partial\Delta\mathbf{u}}{\partial\mathbf{x}_{n+\frac{1}{2}}}\right)^{\mathrm{T}}\right] \tag{80}$$

Then the plastic corrector is derived using the implicit Euler algorithm; and Eq. (72) can be reformulated as,

$$\widetilde{\boldsymbol{\sigma}}_{n+1} = \widetilde{\boldsymbol{\sigma}}_{n+1}^{\text{trial}} - \Delta\bar{\varepsilon}^p \mathbf{E}\mathbf{a}_{n+1} \tag{81}$$

since $\boldsymbol{\Lambda}_\delta = \mathbf{R}_{n+1}\mathbf{R}_{n+1}^{\mathrm{T}} = \mathbf{R}_{n+1}\mathbf{R}_{n+1}^{-1} = \mathbf{I}$.

4.3.2. *Cutting-plane algorithm for stress integration*

Integration of the stress tensor is performed based on Eq. (79) during the current time increment $\Delta t_{n+1} = t_{n+1} - t_n$. The rotated Cauchy stress tensor $\boldsymbol{\Lambda}_\Delta\, \widetilde{\boldsymbol{\sigma}}_n \boldsymbol{\Lambda}_\Delta^{\mathrm{T}}$ from the previous increment and velocity increment tensor $\Delta\mathbf{D}$ are given at the beginning of the time increment at t_n. The stress integration aims to update the stress and internal variables at the end of the current time increment (t_{n+1}).

Suppose the equivalent plastic strain is updated as:

$$\bar{\varepsilon}_{n+1}^p = \bar{\varepsilon}_n^p + \Delta\bar{\varepsilon}_{n+1}^p, \tag{82}$$

The strain rate, temperature, and undamaged stress can be calculated accordingly as,

$$\dot{\bar{\varepsilon}}_{n+1}^p = \Delta\bar{\varepsilon}_{n+1}^p/\Delta t_{n+1}, \tag{83}$$

$$T_{n+1} = T_n + \frac{\varsigma\chi}{\rho C_p}\widetilde{\sigma}_y \Delta\, \bar{\varepsilon}^p, \tag{84}$$

$$\widetilde{\boldsymbol{\sigma}}_{n+1} = \widetilde{\boldsymbol{\sigma}}_{n+1}^{\text{trial}} - \Delta\bar{\varepsilon}_{n+1}^p \mathbf{E}\mathbf{a}_{n+1}, \tag{85}$$

where $\Delta\bar{\varepsilon}_{n+1}^p$ is calculated by meeting the following requirement:

$$F_{n+1}^p = \widetilde{f}(\widetilde{\boldsymbol{\sigma}}_{n+1}) - \widetilde{\sigma}_y(\bar{\varepsilon}_{n+1}^p, \dot{\bar{\varepsilon}}_{n+1}^p, T_{n+1}) = 0. \tag{86}$$

To determine $\Delta\bar{\varepsilon}_{n+1}^p$, the convex cutting plane algorithm proposed by Ortiz and Simo (Simo and Hughes, 2006) is used in this study for stress update as it can bypass the need for the second-order derivative of the yield function for the associated flow rule.

The convex cutting plane algorithm belongs to the elastic-plastic operator split techniques that involve two consecutive steps. In the first step, the current state is assumed to be totally elastic, and the plastic part is frozen. If the trial stress state defined in Eq. (79) is located inside the yield surface (i.e., $F^p(\boldsymbol{\sigma}_{n+1}^{\text{trial}}, \bar{\varepsilon}_n^p, \dot{\bar{\varepsilon}}_n^p, T_n) \le 0$), then the elastic assumption is correct at the current increment $n+1$. Thus, $\Delta\bar{\varepsilon}_{n+1}^p = 0$ and the stress is updated accordingly, $\widetilde{\boldsymbol{\sigma}}_{n+1} = \widetilde{\boldsymbol{\sigma}}_{n+1}^{\text{trial}}$. If the stress state goes beyond the yield surface (i.e., $F^p(\boldsymbol{\sigma}_{n+1}^{\text{trial}}, \bar{\varepsilon}_n^p, \dot{\bar{\varepsilon}}_n^p, T_n) > 0$), the second plastic corrector step attempts to bring back the stress onto the yield surface.

Different from the fully implicit algorithms, the convex cutting plane algorithm is explicit in the sense that the flow rule and hardening law are based on the initial iteration. Assuming $\Delta\bar{\varepsilon}_{n+1}^{p\,(0)} = 0$ and $\widetilde{\boldsymbol{\sigma}}_{n+1}^{(0)} = \widetilde{\boldsymbol{\sigma}}_{n+1}^{\text{trial}}$ as initial conditions, linearisation of the yield function defined in Eq. (86) at the k-th iteration of the $(n+1)$-th increment to correct the plastic strain increment iteratively,

$$F_{n+1}^{p(k+1)} = F_{n+1}^{p(k)} + \mathbf{a}_{n+1}^{(k)} : \delta\boldsymbol{\sigma}_{n+1} - \frac{\partial\widetilde{\sigma}_{y\,n+1}^{(k)}}{\partial\bar{\varepsilon}_{n+1}^{p(k)}}\delta\bar{\varepsilon}_{n+1}^{p(k+1)} - \frac{\partial\widetilde{\sigma}_{y\,n+1}^{(k)}}{\partial\dot{\bar{\varepsilon}}_{n+1}^{p\,(k)}}\delta\dot{\bar{\varepsilon}}_{n+1}^{p\,(k+1)} - \frac{\partial\widetilde{\sigma}_{y\,n+1}^{(k)}}{\partial T_{n+1}^{(k)}}\delta T_{n+1}^{(k+1)} = 0 \tag{87}$$

where $\delta\blacksquare_{n+1} = \blacksquare_{n+1}^{(k+1)} - \blacksquare_{n+1}^{(k)}$. Then, combining Eqs. (83-85), the above equation leads to

$$\delta\bar{\varepsilon}^{p\,(k+1)}_{n+1} = F^{p\,(k)}_{n+1}\Big/\left[\mathbf{a}_{n+1}^{(k)\,T}\mathbf{E}\mathbf{a}_{n+1}^{(k)} - \frac{\partial\widetilde{\sigma}_y{}^{(k)}_{n+1}}{\partial\bar{\varepsilon}^{p\,(k)}_{n+1}} - \frac{\partial\widetilde{\sigma}_y{}^{(k)}_{n+1}}{\partial\dot{\bar{\varepsilon}}^{p\,(k)}_{n+1}}\frac{1}{\Delta t_{n+1}} - \frac{\partial\widetilde{\sigma}_y{}^{(k)}_{n+1}}{\partial T^{(k)}_{n+1}}\frac{\varsigma\chi}{\rho C_p}\widetilde{\sigma}_y{}^{(k)}_{n+1}\right] \tag{88}$$

The iterative procedure is repeated, i.e., $k = k+1$, until the updated yield function reaches a satisfactory value TOL, $F^{p(k+1)}_{n+1}/\tilde{\sigma}^{(k+1)}_{y\,n+1} \leq TOL$. Once the procedure becomes converged, the variables are obtained as: $\blacksquare_{n+1} = \blacksquare^{(k+1)}_{n+1}$. It is worth noting that Chen-Mangasarian or Fischer-Burmeister (FB) replacement functions (Chen and Pan, 2012; Jin et al., 2023) have been employed to smooth complementarity conditions and have been successfully validated in highly cross-linked polymers (Areias et al., 2016), quasi-static frictional and cohesive contact problems (Areias et al., 2013), and the modified Cam-clay model (Zhou et al., 2022). Exploring their applications to dynamic ductile fracture in future studies would be of great interest.

5. Application to additively manufactured metallic materials

This section introduces additively manufactured material samples for validation of crack propagation specimens. The experimental procedure will be then introduced. Lastly, the measurement procedure and calibrated material parameters will be given.

5.1. Material, specimen design and printing scheme

To validate the proposed model, 316L stainless steel was selected as a base material. Laser powder bed fusion (LPBF) was used to print all the following samples via commercial EOS M290 machine (EOS GmbH, Krailing, Germany). Four groups of material specimens, including uniaxial tension (UT), notched tension with a radius of 20 mm (NT), simple shear (SS), and tension specimen with a central hole (CH), as shown in Fig. 2, covering a wide spectrum of stress states, were employed for experimental tests.

Due to scanning direction rotated 67° for each layer, the mechanical properties can be assumed to be transversely isotropic (Li et al., 2023), i.e., being isotropic on the printing plane while anisotropic with respect to the build direction. To characterise this behaviour, material specimens were printed in two orientations, namely, 0° ($y-$ axis) and 90° relative to the build direction ($x-$ axis) in Fig. 2. Moreover, three crack propagation specimens, including the single-notched tension specimen with three holes (SNTT) and the modified second Sandia fracture (MSSF) challenge specimen (see Fig. 3) were used to further demonstrate the capability of the proposed phase field model.

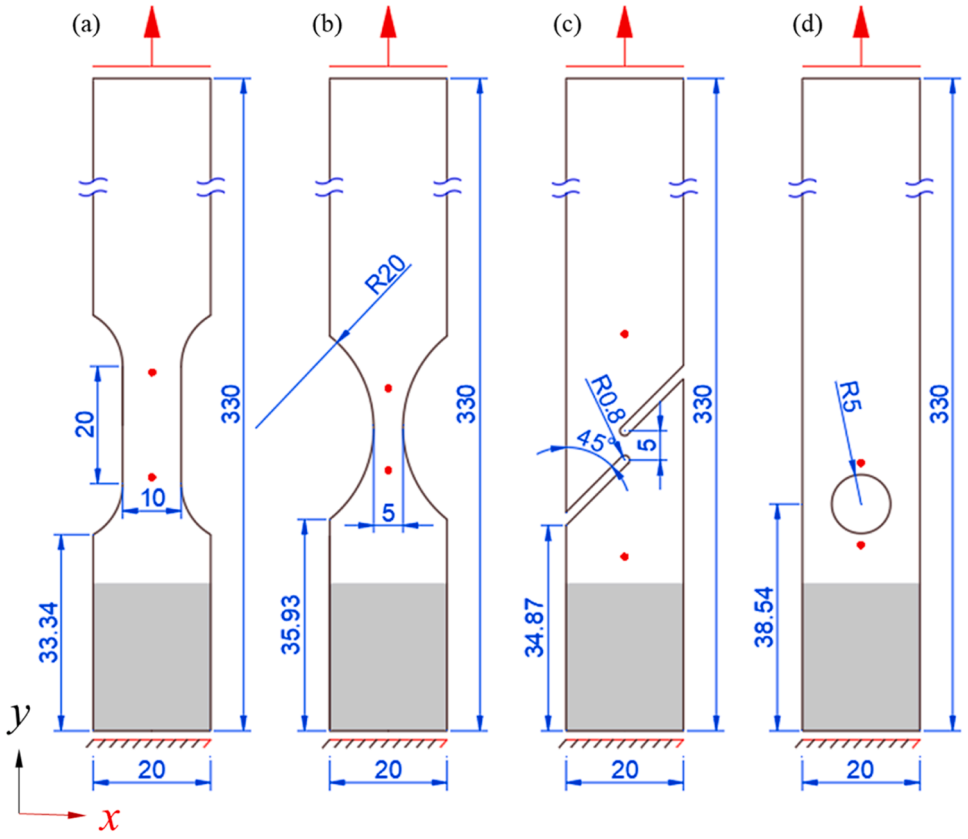

Fig. 2. Specimens for model validation (unit: mm): (a) uniaxial tension (UT), (b) notched tension with a radius of 20 mm (NT), (c) simple shear (SS), and (d) tension specimen with a central hole (CH). The red dots indicate the points to measure the displacement. Those samples were printed in both 0° ($y-$ axis) and 90° relative to the build direction ($x-$ axis) to calibrate the orientation dependent plasticity and fracture models. The specimens involve both orientation and stress state dependencies. The thickness of all the specimens was 1.50 mm.

5.2. Experimental testing of material samples and crack propagation specimens

The samples were tested using Instron VHS 160-20 high speed servo hydraulic testing machine, as shown in Fig. 4. The capacity and maximum speed of the crosshead are 100 kN and 20 m/s, respectively. Meanwhile, a high-speed camera FastCAM was mounted in front of tested samples to capture the whole loading process and measure the strain field using the Digital Image Correlation (DIC) technique. Additionally, experimental data from a Split Hopkinson Pressure Bar (SHPB) (Santiago et al., 2023) was utilised to predict the behaviour of complex triply periodic minimal surface (TPMS) structures under high strain rates in Section 6.3.

5.3. Model calibration

The proposed explicit phase field model contains three groups of material parameters, namely elastoplastic parameters, temperature evolution parameters, and fracture parameters. The parameters for Hill48 yielding function as well as hardening curve under quasi-static loading conditions are referred to our previous work (Li et al., 2023). Correspondingly, $\dot{\bar{\varepsilon}}_0$ was set as 0.0028 s^{-1}, as per strain rate under quasi-static testing. As for the strain rate dependency, all the 90° UT specimens under different loading velocities were used to calibrate the modified Johnson-Cook model, i.e., C_0 and C_1. The room temperature T_{room} and melting temperature T_{melt} were 20.0 °C and 1398.0 °C (Li et al., 2020a), respectively. Concerning thermal softening parameter m, the inverse identification was used by minimising the numerical and experimental force-displacement response for all the material specimens (Li et al., 2020a). The elastoplastic parameters are given in Table 1.

In terms of temperature evolution, the thermal parameters, e.g. heat capacity, Taylor–Quinney coefficient, and adiabatic limit strain rate, were obtained from the literature (Li et al., 2020b). In this study, to better describe the LPBF printed 316L specimens, the material parameters were slightly modified via the inverse identification (Li et al., 2020a). As a result, the calibrated material parameters are given in Table 2.

Due to transversely isotropic mechanical properties in LPBF printed metallic materials (Li et al., 2023), β_{xx} and β_{zz} are set to be 1 because ε^p_{xx} and ε^p_{zz} contribute equally and serve as the reference for ε^p_{yy}. Similarly, β_{xz} and β_{yz} are also set to be 1 because ε^p_{xz} and ε^p_{yz} contribute equally and serve as the reference for ε^p_{xy}. When $\beta_{yy} = \beta_{xy} = 1$, $\bar{\varepsilon}^{p,\ ani}$ reduces to the equivalent plastic strain defined in Eq. (29). Basically, the anisotropy is introduced by distinguishing the contributions of each component of the plastic strain tensor. Suppose that β_{yy} is a very large value, the MMC may be triggered even if the plastic strain in z direction is small. The material parameters for Modified Mohr-Coulomb (MMC) model were taken from Li et al. (2023). The parameters for linear transformation were calibrated using all material samples to minimise the deviation of the numerical and experimental fracture initiations. As for damage evolution, the length scale parameter was set as 0.2 mm to regularise the sharp crack and match the experimental data.

The critical energy release rate g_f was determined by referring to Margerit et al. (2021). Note that g_f can vary with stress state (Chu

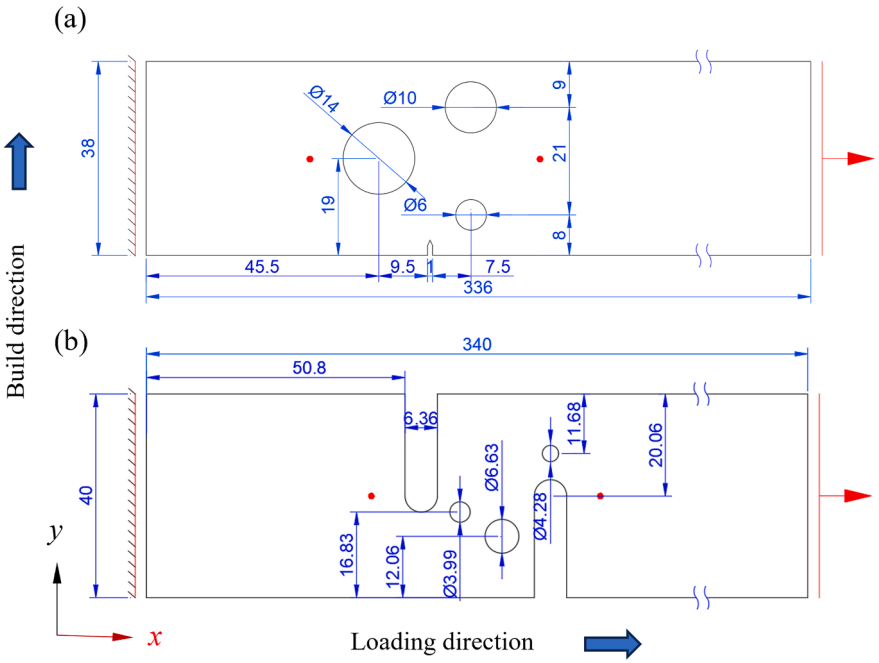

Fig. 3. Crack propagation specimens (unit: mm): (a) single-notched tension specimen with three holes (SNTT); (b) modified second Sandia fracture (MSSF). The red dots specify the points to measure the displacement. Those samples were printed in 90° relative to the build direction (x − axis) for validating the proposed model. The thickness of SNTT was 1.50 mm, while for MSSF was 3.12 mm to avoid out-of-plane bending deformation.

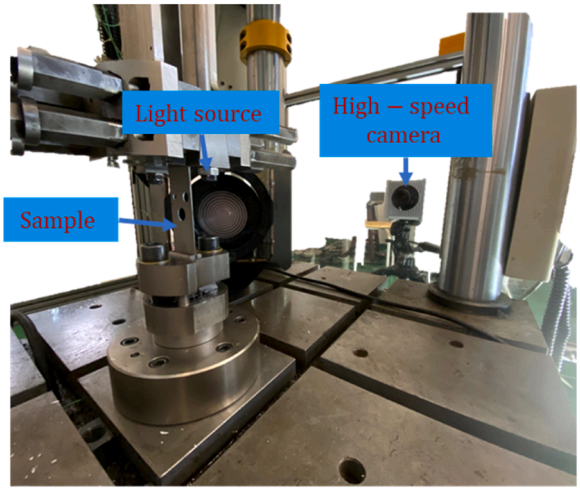

Fig. 4. Experimental setup. Instron VHS 160-20 high speed servo hydraulic machine were used to conduct high-speed test and record the global force. Meanwhile, the FastCAM camera was employed to capture the deformation process.

Table 1
Orientation, strain rate, and temperature dependent elastoplastic parameters

Types	Parameters	Physical meaning	Value
Elasticity (Li et al., 2023)	$\widetilde{E}$	Elastic modulus	145.0 GPa
	ν	Poisson's ratio	0.3
Hill48 model (Li et al., 2023)	F	Transversely isotropic yield function	0.5
	G		0.39
	H		0.5
	L		1.5
	M		1.5
	N		1.45
Modified Johnson-Cook model	C_0	Strain rate hardening parameters	0.0312
	C_1		-3.412
	$\dot{\bar{\varepsilon}}_0$		0.0028 s^{-1}
	m	Thermal softening parameter	0.921

Table 2
Parameters for temperature evolution

Type	Parameters	Physical meaning	Value
Temperature evolution	C_p	Heat capacity	460 J/(kg·°C)
	χ	Taylor–Quinney coefficient	0.7
	$\dot{\varepsilon}_a$	Adiabatic limit strain rate	1.5 s^{-1}

et al., 2019) and strain rate (Borges et al., 2020). In this study, however, g_f was considered as a constant for simplicity, yet it would be an intriguing topic to investigate the influence of g_f on phase field models in the future studies. The fracture parameters are shown in Table 3.

6. Results and discussion

This section compares the experimental and numerical results to assess the performance of the proposed explicit phase field model. In particular, the strain rate, orientation, and stress state dependencies will be evaluated via the sample tests, i.e., uniaxial tension (UT), simple shear (SS), notched tension (NT), and tensile specimen with a central hole (CH). Furthermore, crack propagation specimens, involving complicated crack initiation and propagations, will be also used to demonstrate the capability of the proposed model in complex scenarios. Lastly, TPMS Dimond (D) structures under impact loading with different volume fractions are simulated, with fracture mechanisms analysed.

Table 3
Parameters for fracture initiation and propagation

Types	Parameters	Physical meaning	Value
Damage initiation (Li et al., 2023)	A	MMC fracture model	1338.87 MPa
	n		0.7
	c_1		0.01
	c_2		465.69 MPa
	c_3		0.74
	b_0	Rate dependency	0.66
	γ		0.025 s
	$\dot{\varepsilon}_0$		0.00185 s^{-1}
	β_{xx}	Orientation dependency	1.00
	β_{yy}		0.20
	β_{zz}		1.00
	β_{xy}		1.5
	β_{yz}		1.00
	β_{zx}		1.00
Damage evolution	l_c	Length scale parameter	0.2 mm
	g_f	Critical energy release rate	15 N/mm

6.1. Material-level samples

6.1.1. Strain rate dependency

To illustrate the strain rate dependency, the force-displacement curves of the 90° uniaxial tension sample under loading velocities of 0.3, 1, 4, 8, and 14 m/s are presented in Fig. 5. The corresponding nominal strain rates are 16.7, 55.6, 222.2, 444.4, and 777.8 s^{-1}, respectively. Evidently, the simulation can properly reproduce the experimental results in terms of initial elastic stages, plastic hardening, and fracture initiations and propagations of all the five loading scenarios.

Note that the flow stress increased with the strain rate. For example, when the nominal strain rate increased from 16.7 to 777.8 s^{-1}, the yield stress increased from 666.7 to 933.3 MPa (or equivalently the corresponding force increased from 10 to 14 kN). Furthermore, it is observed that the simulated flow stress agreed well with the experimental data, indicating the accuracy of the modified Johnson-Cook model in Eq. (30).

The effect of strain rate on crack initiation was relatively more complicated. According to the experimental data, when the strain rate increased from 16.7 to 55.6 s^{-1}, the displacement to fracture was reduced from 6.4 to 5.7 mm. The simulated results slightly overestimated the ductility of the samples when the strain rate was smaller than 55.6 s^{-1}. When the strain rate ranged from 55.6 to 777.8 s^{-1}, the ductility became less insensitive to strain rate, which was properly captured by the numerical model, as shown in Fig. 6c-e. The nonlinear relationship between the strain rate and fracture strain was reported by Li et al. (2019). Overall, the prediction of the influence of strain rate on fracture initiation was acceptable, with the average relative error being around 4.5%, showing a sufficient accuracy of the strain rate dependent MMC model in Eq. (37).

The contours of the equivalent plastic strain $\bar{\varepsilon}^{p,\ ani}$ at the instant of fracture initiations with loading speeds of 0.3, 1, and 14 m/s were also provided in Fig. 6, in which the strain localisation could be observed in the middle region. The maximum $\bar{\varepsilon}^{p,\ ani}$ significantly reduced from 0.51 to 0.44 when the nominal strain rate increased from 16.7 to 55.6 s^{-1}; but it slightly reduced from 0.44 to 0.40 when the nominal strain rate increased from 55.6 to 444.4 s^{-1}. It implies that the ductility was less sensitive to strain rate when strain rate ranged from 55.6 to 444.4 s^{-1}. Moreover, the temperature fields at the instant of fracture initiation are also provided in Fig. 6. With a higher loading speed, the maximum temperature tended to reduce due to smaller plastic deformation to initiate fracture.

Regarding the damage evolution, the simulated force-displacement curves showed similar decreasing rates with the experimental counterparts in Fig. 5, indicating the accuracy of the proposed phase field model. Moreover, the horizontal crack paths were well captured, as shown in Fig. 6.

To elucidate the strain rate dependency, Fig. 7 displays the evolution of equivalent plastic strain, flow stress, strain rate, temperature, damage indicator, and phase field of critical elements. According to the evolution of $\bar{\varepsilon}^{p,\ ani}$ in Fig. 7a, two stages of loading, namely homogeneous deformation and localised deformation, can be observed.

In the first stage, with the displacement between gauges sections being smaller than 2.8 mm, $\bar{\varepsilon}^{p,\ ani}$ presented good consistency even under varied loading velocities, suggesting their homogeneous response. The strain rates increased with loading velocities, whereas temperatures remained nearly same, as show in Fig. 7b. According to Eq. (25), thermal evolution was driven by equivalent plastic strain, while equivalent plastic strain did not differ significantly due to homogeneous response, resulting in that temperature was relatively insensitive to strain rate in this stage. Flow stresses also rose with loading velocities, primarily due to strain rate hardening, as deduced from Eq. (30).

However, when displacement between the gauges sections exceeded 2.8 mm, equivalent plastic strain, strain rate, and temperature started showing rising differences, signifying localised deformation. Plastic localisation and thermal softening were coupled as per Eq. (30), possibly leading to significant sensitivity to loading velocities. In contrast, flow stress showed less sensitivity to loading velocities, attributing to insensitivity to equivalent plastic strain and a compromise between strain rate hardening and thermal softening.

Interestingly, damage indicator exhibited remarkable differences even from the homogeneous stage. This can be attributed to the

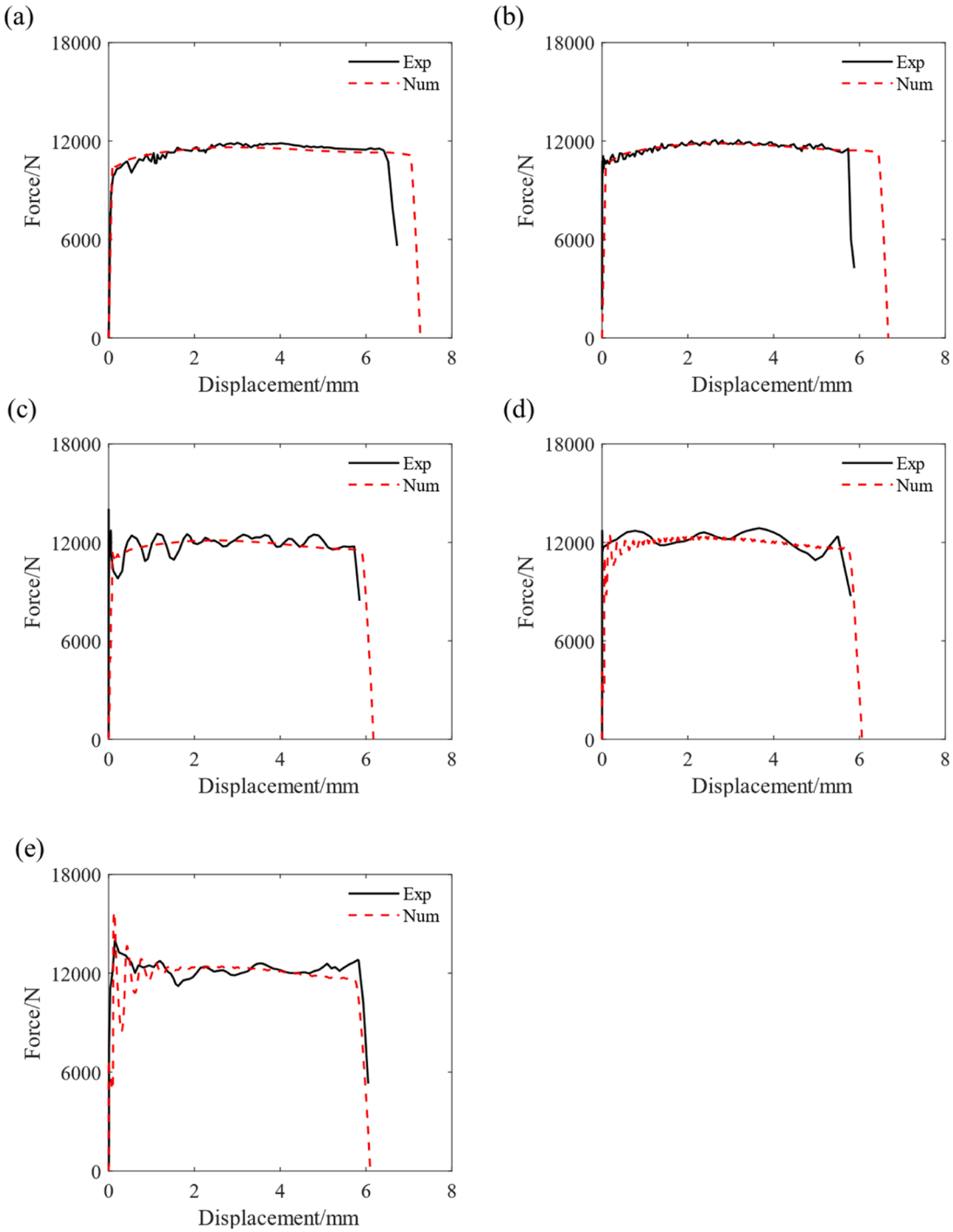

Fig. 5. Force-displacement curves of the 90° UT samples under different loading velocities. (a) 0.3 m/s; (b) 1 m/s; (c) 4 m/s; (d) 8 m/s; (e) 14 m/s. Displacements were measured in the gauge section, as highlighted in Fig. 2. The flow stress increased with strain rate.

definition of damage indicator in Eq. (34). Firstly, due to fracture strain was rate dependent as in Eq. (32), the fracture strains were approximately 0.445, 0.435, and 0.398 for samples with loading velocities being 0.3 m/s, 1 m/s, and 14 m/s, respectively. Secondly, the equivalent plastic strain showed notable differences in the localised stage. After fracture initiations, phase field evolved from 0 to 1, representing material point transitioning from intact to broken state.

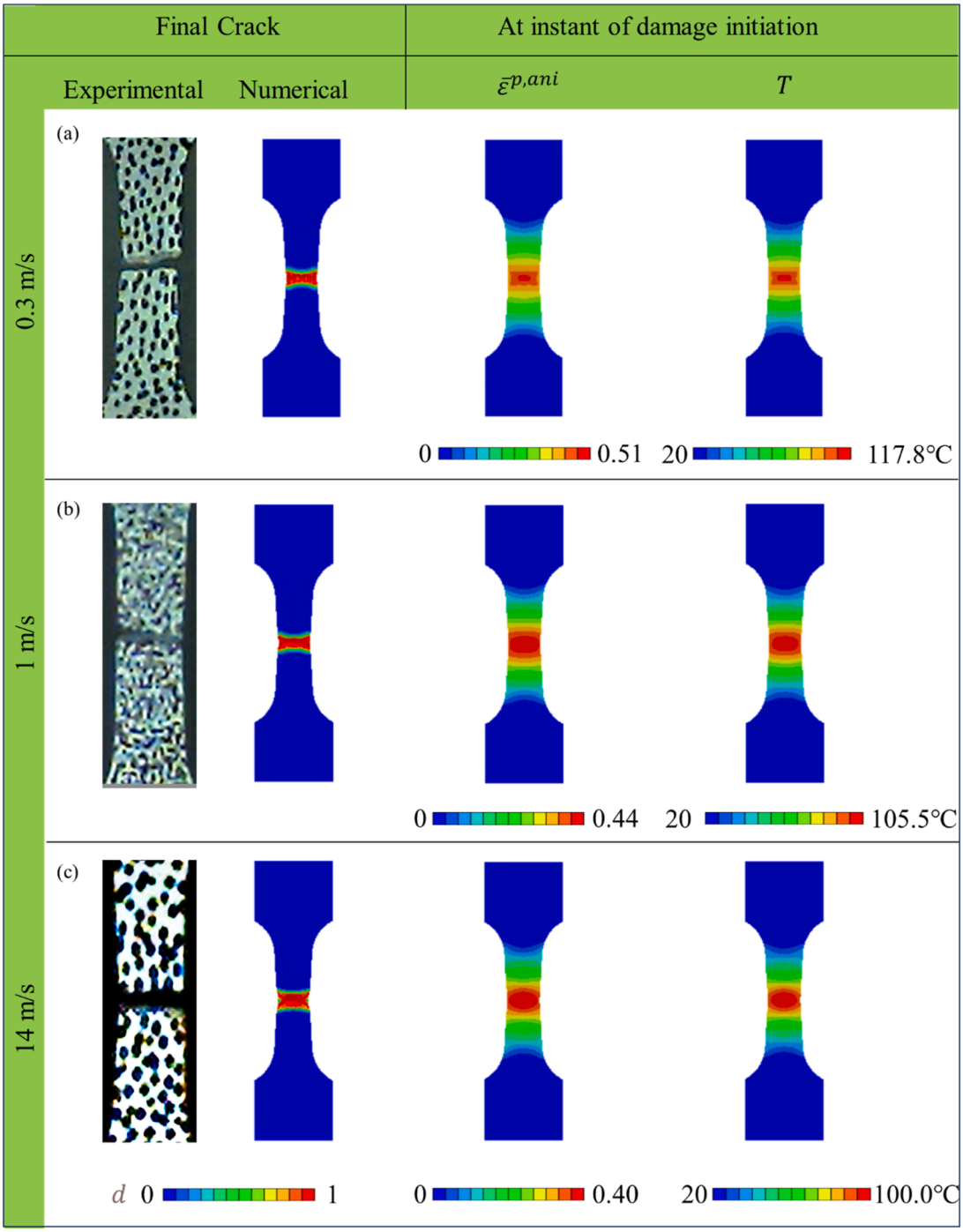

Fig. 6. Final crack paths and numerical contours of equivalent plastic strain and temperature. (a) experimental and numerical cracks at the end of loading; (b) $\bar{\varepsilon}^{p,\ ani}$; and (c) temperature at the instant of damage initiation.

6.1.2. Stress state dependency

Fig. 8 presents the force-displacement response of the notched tension specimen (NT), the tensile specimen with a central hole (CH), and the simple shear (SS) with a loading velocity of 1 m/s. Apparently, the experimental global responses before fracture initiations were properly simulated by the proposed method, indicating the accuracy of the elastoplastic model, with the average error for this group of specimens being only 4%.

Furthermore, the damage evolutions could be properly predicted, as shown in the descending branches in Fig. 8. The simulated crack paths were in good agreement with the experimental data, as shown in Fig. 9. At the instant of damage initiation, simple shear

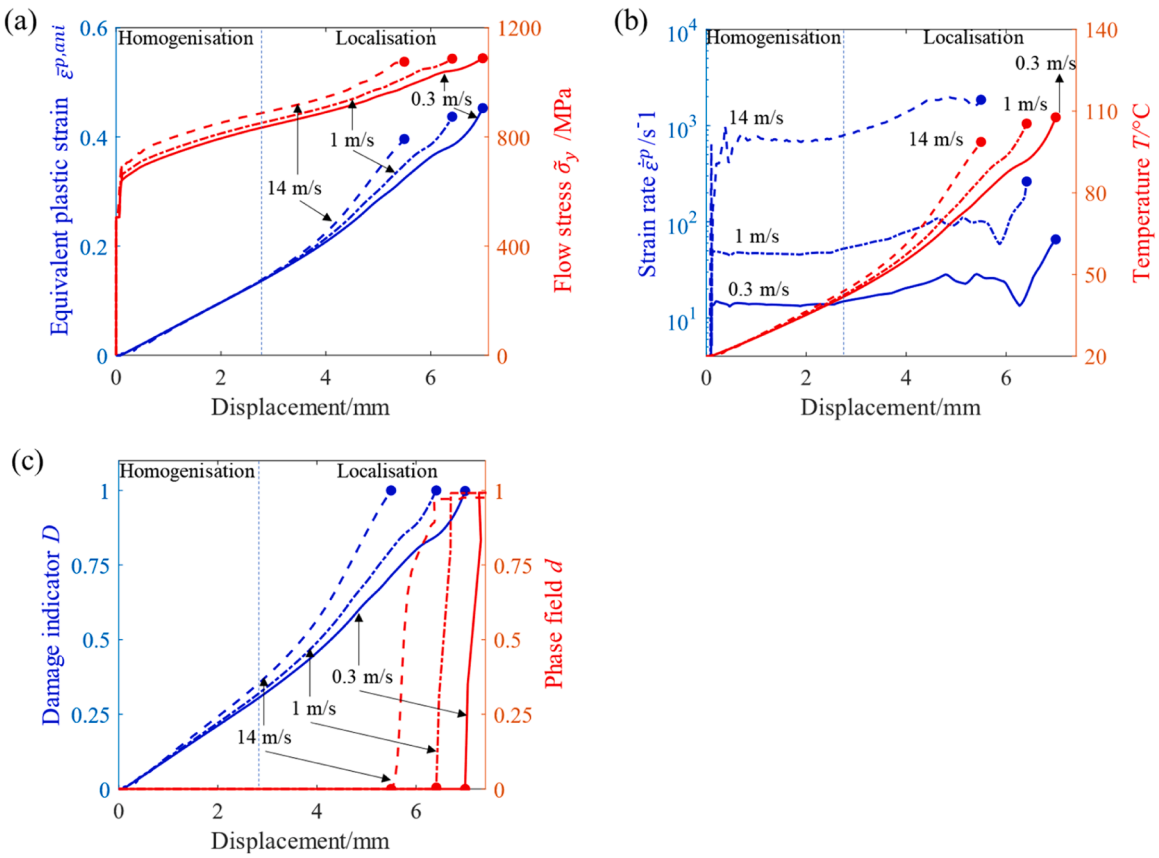

Fig. 7. Numerical results of critical element under loading velocities of 0.3 m/s, 1 m/s, and 14 m/s. Evolution of (a) equivalent plastic strain and flow stress; (b) strain rate and temperature; (c) damage indicator and phase field.

specimen required remarkably higher equivalent plastic strain than that in the NT or CH specimens, as evidenced in Fig. 9, indicating that the influence of stress state on fracture strain should be considered. The distributions of temperature were almost identical to the equivalent plastic strain simply due to the way of heat conversion from plastic deformation (see Eq. (25)). At the instance of fracture initiation, although the NT sample did not exhibit the highest equivalent plastic strain, it had the highest strain rate that induced the highest flow stress, leading to its highest temperature. In addition, the critical elements to initiate the fracture in these specimens covered a wide range of stress states, as presented in Fig. 10 and discussed later.

The fracture envelope together with loading histories of critical material points are presented in Fig. 10. Although the strain rates were different for the material points at the instant of damage initiation, they did not differ significantly. Therefore, the fracture envelope was plotted based on their average strain rate, i.e., 420 s^{-1}. The stress states $(\eta, \bar{\theta})$ at the instant of damage initiation for UT, NT, SS, and CH were $(0.36,\ 0.90)$, $(0.45,\ 0.72)$, $(0.06,\ 0.18)$, and $(0.35,\ 0.98)$, respectively. Their corresponding equivalent plastic strain to fracture were 0.43, 0.44, 0.51, and 0.41. The fracture strain tended to be larger for shear loading, which was consistent with the result in quasi-static loading (Li et al., 2023). This means that it is still essential to consider the influence of stress states on fracture initiation under dynamic loading. It should be pointed out that the damage initiation points are found to be located almost on the fracture envelope due to proportional loading histories of the critical material points (Luo et al., 2012).

6.1.3. Orientation dependency

Fig. 11 displays the force-displacement curves of the 0° specimens including UT, NT, and CH with a loading velocity of 1 m/s. Prior to damage initiations, both the transversely isotropic and isotropic fracture models yielded the same results due to the same elasto-plastic constitutive relation and material parameters. In terms of damage initiations, however, the relative errors of the isotropic fracture model were 14.9%, 15.4%, 25.2%, respectively. The relative error was reduced to 1.9%, 8.1%, and 6.4%, respectively, after introducing the linear transformation in Eq. (35). The accumulation of damage indicator is adjusted such that the orientation dependent fracture initiation could be properly simulated. In conclusion, although the predicted crack paths were correct using the isotropic fracture initiation model, it remains necessary to use the transversely isotropic one to achieve accurate force-displacement responses. The influence of anisotropic fracture initiation on crack paths will be further demonstrated in the next section.

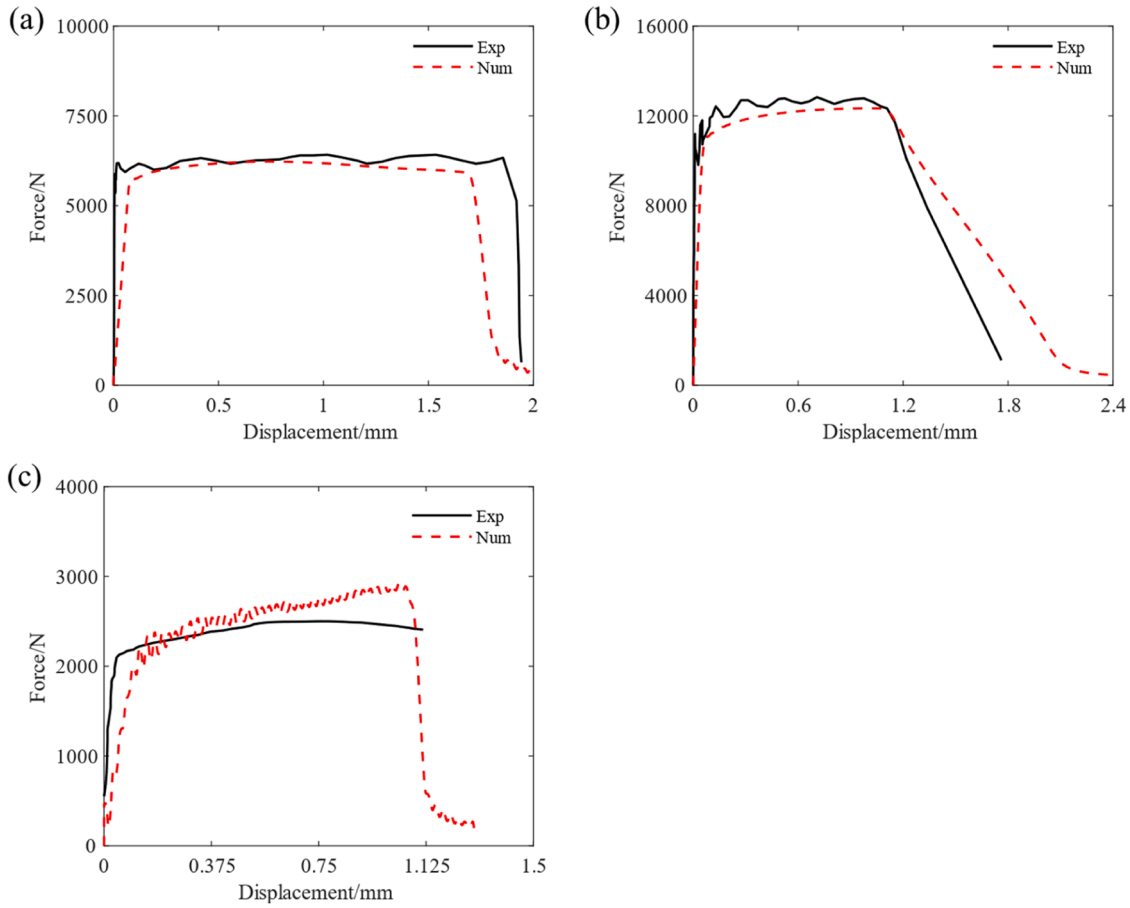

Fig. 8. Force-displacement curves for (a) the notched tension specimen NTR20, (b) the tensile specimen with a central hole CH20, and (c) the simple shear SS. Displacements were measured in the gauge section, as highlighted in Fig. 2.

6.2. Crack propagation specimens

6.2.1. Single-notched tension specimen with three holes

Fig. 12 compares the numerical and experimental force-displacement curves of the single-notched tension specimen with three holes under loading velocities of 0.3 and 4 m/s. Apparently, the simulation properly replicated the experimental results. Also, the strain rate hardening could be observed in the simulation. It is noted that the crack paths were insensitive to loading velocities. Therefore, samples loaded with a speed of 0.3 m/s were selected to provide a detail deformation process.

Based on the force-displacement curves, there were five characteristic stages in the whole loading process. In the first stage, the global force increased sharply until reaching the peak load due to elastoplastic deformation, as shown in Fig. 12. The simulated force was in good consistency with experimental data. There were no visible cracks in this stage from both the experimental and numerical results.

In Stage II, the global force gradually decreased. The simulation made a good prediction to the experimental results. Furthermore, the crack started propagating from A towards the left due to medium stress triaxiality tension in the simulations, as presented at instant ii in Fig. 13. However, there was a non-negligible crack propagating from hole D to E in the numerical result, which was ahead of the experimental observation. The discrepancy may be caused by heterogeneous mechanical properties induced by 3D-printing (Kok et al., 2018). Nevertheless, due to the small section area between D and E, the discrepancy of crack formation did not lead to an unacceptable force-displacement diagram.

In Stage III, the simulated force was higher than its experimental counterpart. The discrepancy was mainly due to a crack between A and B. In the experiment, the crack propagation was much earlier than the simulation. Also, the experimental crack developed in the horizontal direction, whereas the simulated crack tended to develop in an inclined direction, noting the formation of crack on the right side of hole B. It is noted that the crack initiations at A and B were caused by high stress triaxiality tension and uniaxial tension, respectively.

In Stage IV, the simulated force was still higher than the experimental data due to the inconsistent crack path in the last stage. Due to crack initiations on A and B in the last stage, the simulated crack merged from both A and B to the middle region. Nevertheless, the

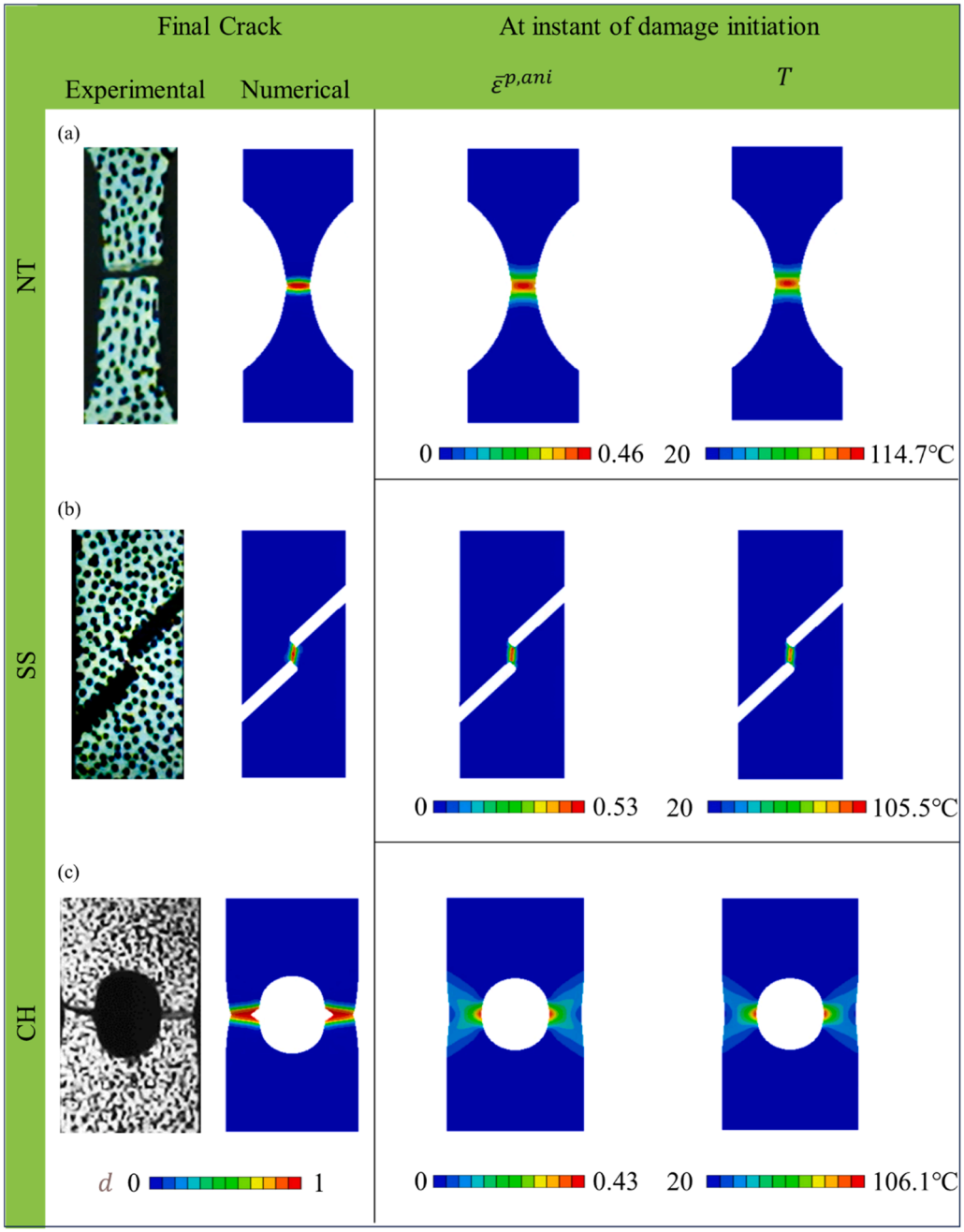

Fig. 9. Crack paths and numerical contours. Crack paths could be well captured. The critical equivalent plastic strains were different under different stress states, strengthening the necessity of considering stress states.

crack between A and hole B experienced a complete rupture in both the experiment and simulation, resulting in good agreement of force at the end of this stage.

In Stage V, the global force remained stable albeit with slight fluctuation due to dynamic effect (Jones, 2011), as shown in Fig. 12. The numerical model presented a pretty high accuracy in this stage. Crack initiated between D and B due to the shear and tension-shear stress states. Then, the cracks propagated from holes D to B in both simulation and experiment.

During the loading process, there were compressive areas such as the bottom and top of hole B. They fall in the compressive cut-off region. As a result of introducing a cut-off value for stress triaxiality here, the compressive damage was suppressed. With the phase field methods, strain-based (Amor et al., 2009; Miehe et al., 2010a) or energy-based decompositions (Miehe et al., 2010b) techniques were frequently adopted to avoid compressive damage. In this study, with introduction of a cut-off value for stress triaxiality, complicated strain or energy decomposition can be avoided.

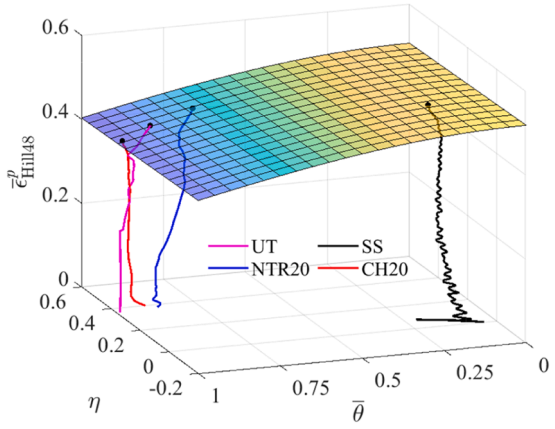

Fig. 10. Fracture envelope and loading histories of critical material points. The fracture strains were stress states dependent. Also, all the loading histories of the critical material points were nearly proportional.

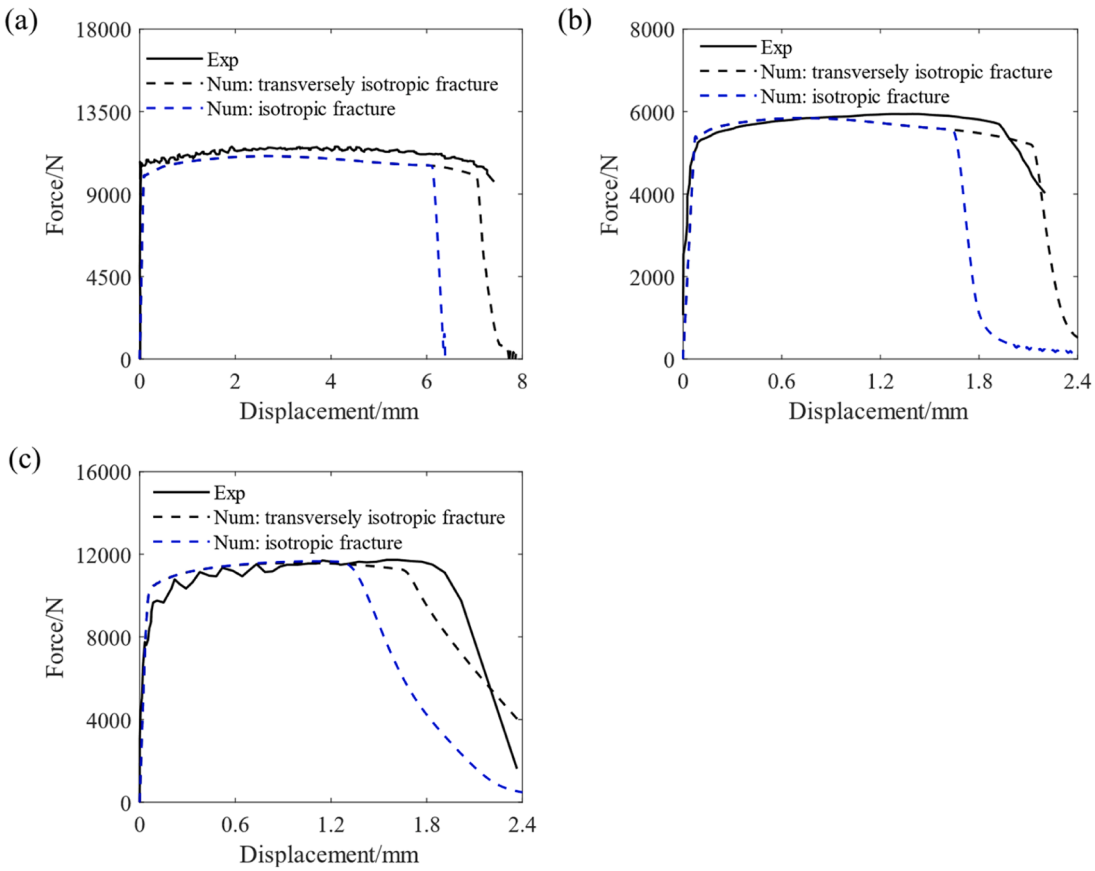

Fig. 11. Force-displacements curves of the 0° specimens. (a) UT; (b) NT; (c) CH. Displacements were measured in the gauge section, as highlighted in Fig. 2. Here, the Isotropic fracture initiation model led to considerably larger errors than the transversely isotropic counterpart.

6.2.2. Modified second Sandia fracture challenge specimen

The experimental and numerical force versus displacement data of the modified second Sandia fracture challenge sample are compared in Fig. 14. Overall, the phase field model with transversely isotropic fracture model exhibited good prediction for the experimental results under loading speeds of 0.3 and 8 m/s. While the crack paths were not sensitive to loading velocity, the influence of strain rate on global response can be observed. Given a higher loading velocity, the strength was increased due to the strain rate induced hardening effect, while ductility was reduced, which showed the same pattern as material samples. To provide a

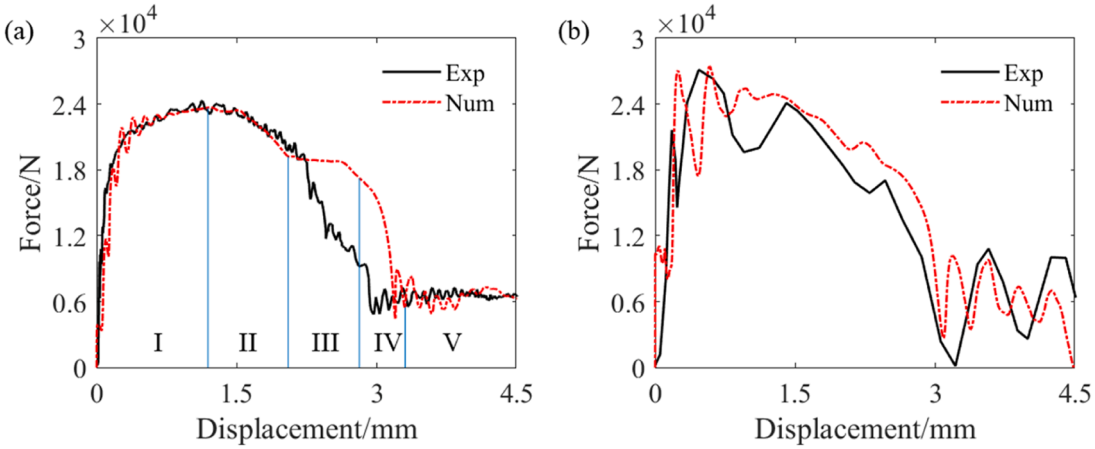

Fig. 12. Force-displacement curves for single-notched tension specimen with three holes. (a) 0.3 m/s; (b) 4 m/s.

comprehensive analysis of crack propagation, the global response of samples with a loading speed of 0.3 m/s was divided into six stages as illustrated in Fig. 14.

The numerical and experimental deformation are compared in Fig. 15. To facilitate the following description, two notches are labelled with A and D, three holes of different sizes with B, E and F, and the left edge with C, as presented in Fig. 15.

The global force increased linearly in the beginning and then levelled off somewhat until reaching the peak load in Stage I, which was typically associated with elastoplastic deformation. The simulated force-displacement responses agreed well with the experimental counterparts, revealing the accuracy of the proposed elastoplastic model.

Stage II experienced in a sudden load drop due to crack formation from A to B, as depicted in Fig. 15. The crack was triggered by medium and high stress triaxiality tension. Note that the simulated crack was slightly earlier than the experimental counterpart, probably due to increased thickness in 3D printing (Smith et al., 2021). Nonetheless, the relative error was acceptable in such dynamic loading scenarios.

Stage III was characterised by a plateau in both numerical and experimental curves, as presented in Fig. 14, which could be a compromise of plastic hardening, strain rate hardening, thermal softening, and damage degradation in this stage. The simulation properly reproduced the experimental data in terms of global deformation and force-displacement response despite complicated phenomena.

In Stage IV, the numerical and experimental forces reduced gradually due to crack formation between D and E (see the experimental and numerical results with transversely isotropic fracture model in Fig. 15), which were triggered by medium stress triaxiality tension and tension-shear. Meanwhile, the cracks between B and C could be observed in both the simulation and experimental data. The crack was mainly induced by a high stress triaxiality tension. Interestingly, a minor crack can be noted on the right side of D in the numerical model with a transversely isotropic fracture initiation model. The crack between D and E was dominant, and thus the horizontal crack propagation around D was suppressed. However, if the isotropic fracture model was used, the horizontal crack was dominant over the crack between the D and E, which can be explained by the contours of the equivalent plastic strain. The strain localised horizontally if neglecting the influence of printing orientation on fracture initiation, thereby leading to unacceptable errors in the force-displacement curve and crack paths, as shown in Fig. 14 and Fig. 15.

Stage V underwent gradual and abrupt load drop in a sequential manner, as shown in Fig. 14. The gradual drop was caused by crack propagation between E and F. After its full rupture, the global force reduced significantly due to dramatically reduced cross-sections that could bear the external load (see Fig. 15).

The global force remained nearly unchanged in Stage VI in both the experiment and simulation. The rest of uncracked regions, i.e., the right side of C and the upper area of F, still bore the external loads. The numerical results showed good consistency with the experimental data, indicating the capability and effectiveness of the proposed model.

6.3. TPMS structures

Lastly, TPMS D structures under impact loading were used to further validate the proposed model. The illustration of D structure and its unit cell are presented in Fig. 16a. Experimental data was taken from (Santiago et al., 2023), where a Split Hopkinson Pressure Bar (SHPB) was employed to perform dynamic compressive tests. The 316L steel samples were printed using an EOS M290 printer, identical to the one used in this study. Therefore, the material parameters in Tables 1, 2, and 3 remained suitable for simulation.

The TPMS D lattices with voxel elements were generated by a MATLAB code (Li et al., 2024). The total number of elements (Li et al., 2024) in the displacement layer were approximately 329,000, 417,000, and 546,000 for the D structures with volume fractions of 27%, 34%, and 45%, respectively, resulting in total degrees of freedom of 4.25 million, 4.82 million, and 5.68 million. In line with (AlMahri et al., 2021; Santiago et al., 2023), the dynamic compressive loading was simulated by a striker with a mass of 0.9 kg and an impact velocity of 33 m/s.

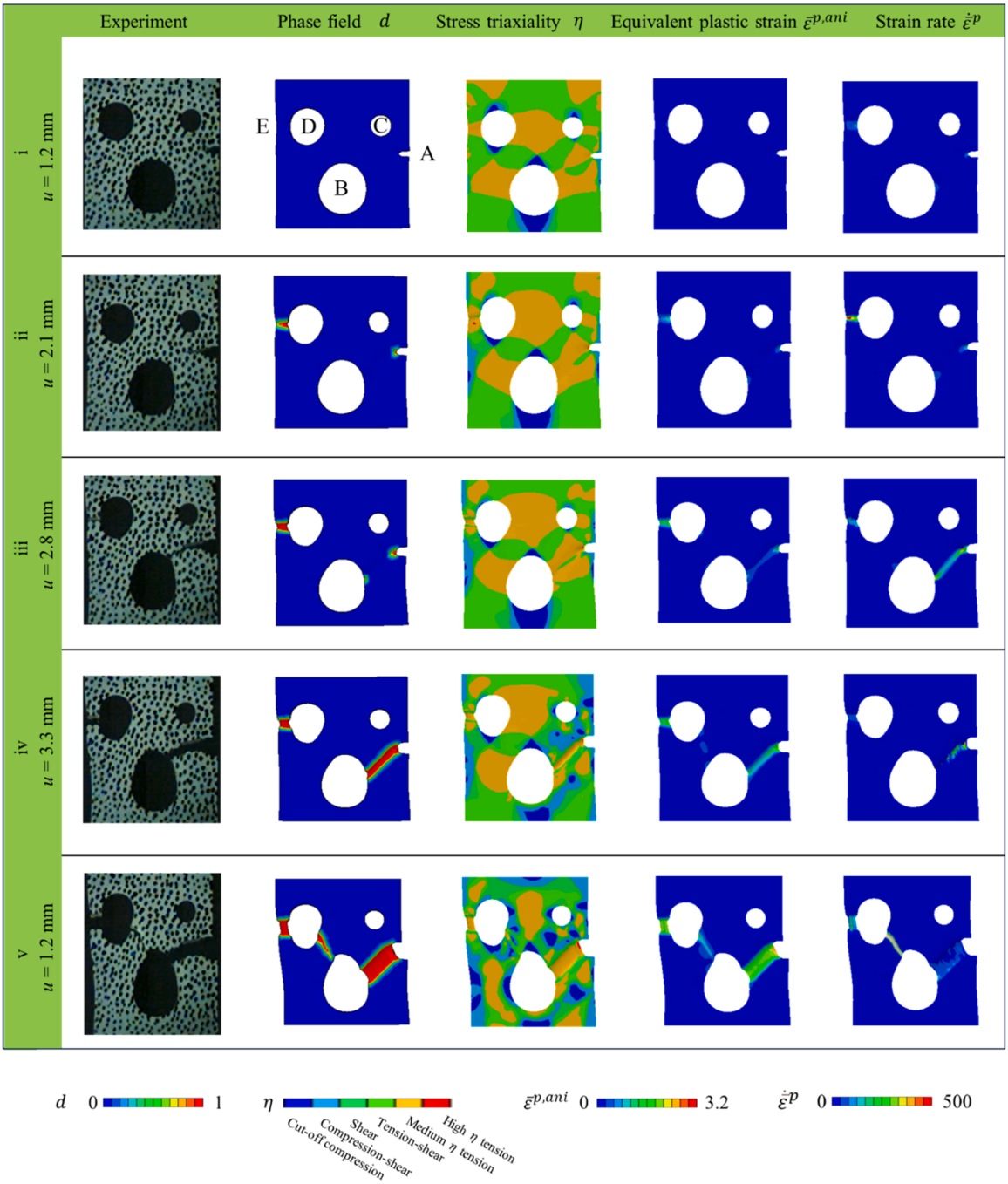

Fig. 13. Experimental and numerical comparison of the single-notched tension specimen with three holes. The overall crack path can be predicted properly, albeit with a slight discrepancy of cracks in between D and E and inclined crack between A and B. The definition of stress state can be found in Section 3.2.

6.3.1. *Force-displacement response*

Fig. 16b compares simulated and experimental stress-strain curves for D structure with different volume fractions. As the volume fraction increased, the simulated nominal stress also increased, agreeing with the experimental results. The initial peak and plateau stress could also be properly predicted by the proposed phase field model, with initial peak stress increased from 105 MPa to 140 MPa and 185 MPa for the three volume fractions. The experimental deformation modes were well captured by the numerical model, as depicted in Fig. 16c-e. For example, densification was evident for the 27% volume fraction due to its lower load-bearing capacity, whereas the D structure with 45% volume fraction showed no densification, indicating it did not require densification to absorb the

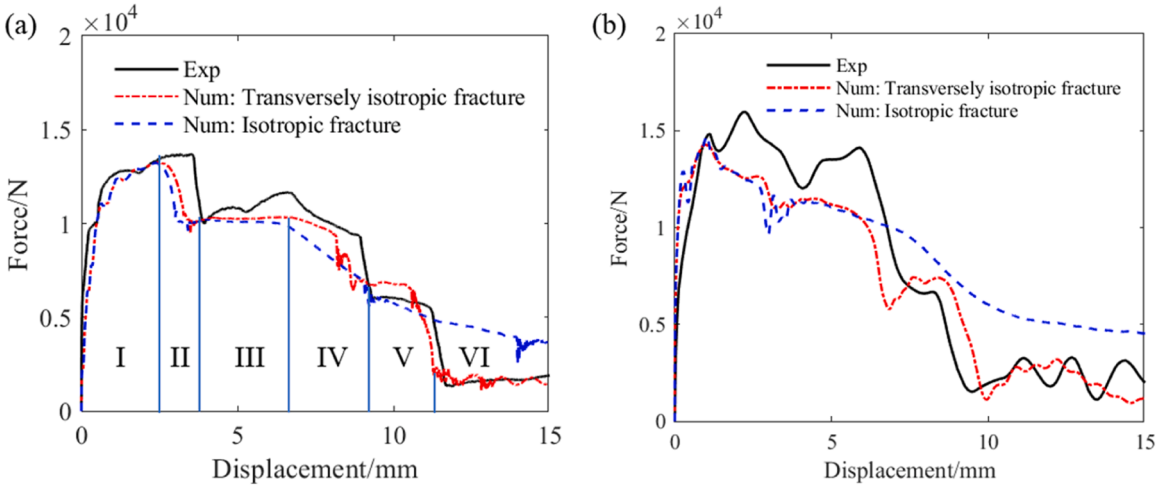

Fig. 14. Force-displacement curves for the modified second Sandia fracture challenge specimen. (a) 0.3 m/s; (b) 8 m/s.

input energy.

More importantly, cracks could be well captured by the phase field model. Take D structure with 27% volume fraction as an example, as shown in Fig. 16f, crack initiated at the corners, followed by crack initiation and propagation in the central region. In the end, cracks further developed and merged, forming vertical strip-shaped cracks. Distributed rather than localised shear failure was observed owing to the excellent mechanical performance of TPMS structures. Detailed fracture mechanism analysis will be discussed for all three volume fractions in the next section.

6.3.2. Fracture mechanism

To compare the fracture mechanism of D structures with different volume fractions, the stress triaxiality and Lode angle parameter at the instant of damage initiation ($D = 1$) and fully rupture ($d = 1$) were extracted from numerical results. Fig. 17a depicts that the percentages of partially damaged and fully ruptured material points reduced with volume fractions, indicating enhanced fracture resistance with higher volume fractions. According to Fig. 17b, compression-shear and shear were the dominant stress states for the damage of all the D structures, followed by tension-shear loading, while the medium and high stress triaxiality tensions were minimal. Although localised global shear bands did not form (Fig. 16c-e), shear failure was distributed across the cracked regions.

Figs. 17c-e show the stress state heatmaps for all the elements at the instant of damage initiation for the three volume fractions. In addition to the primary shear-related damages common to all three D structures, the 27% volume fraction exhibited more tension-induced damage initiation. For example, more material points experienced stress states close to uniaxial and equibiaxial tensions. This can be attributed to the lower volume fraction, which facilitated local buckling and bending of the walls, thereby increasing tension-induced damage. Due to cut-off value introduced in Eq. 37, compressive damage was suppressed when stress triaxiality was smaller than -1/3, which proved to be an alternative to complex strain decomposition methods (Amor et al., 2009; Miehe et al., 2010b).

7. Conclusions

To simulate dynamic ductile fracture, this study proposed an explicit phase field modelling framework. The governing equations in both weak and strong forms were formulated using the variational principle. Strain rate and temperature dependent plastic behaviour was described by a modified Johnson-Cook model. Fracture initiation was described by the strain rate dependent Modified Mohr-Coulomb model (MMC) to capture both strain rate and stress state dependency. Furthermore, to predict orientation dependency, transversely isotropic Hill48 yielding function and MMC models were used.

To validate the proposed model, a series of material samples were tested for calibration purposes. The calibrated results revealed that a higher strain rate led to higher strength yet lower ductility, which was in good agreement with the experimental observation. In addition, the fracture strains varied under different stress states. Therefore, it is necessary to consider stress state dependency in fracture initiations. Last, due to the characteristics of 3D printing process, plastic behaviour and fracture initiation exhibited orientation dependency. 0° material specimens were used to demonstrate that orientation dependent fracture initiation should be considered to achieve acceptable prediction accuracy.

Crack propagation specimens were tested to further demonstrate the capability of the proposed explicit phase field model. Although complicated crack paths were involved, force-displacement curves and crack paths under different loading velocities can be simulated properly. Importantly, tests of the modified Second Sandia Fracture Challenge specimens revealed that it was indispensable to consider the transversely isotropic model for predicting fracture initiation. Otherwise, the crack paths could be incorrectly predicted with the isotropic fracture model, leading to unacceptable errors in force-displacement curves. Last, the proposed phase field model was employed to simulate TPMS D structures under impact loading. The global nominal stress-strain response, deformation mode, and

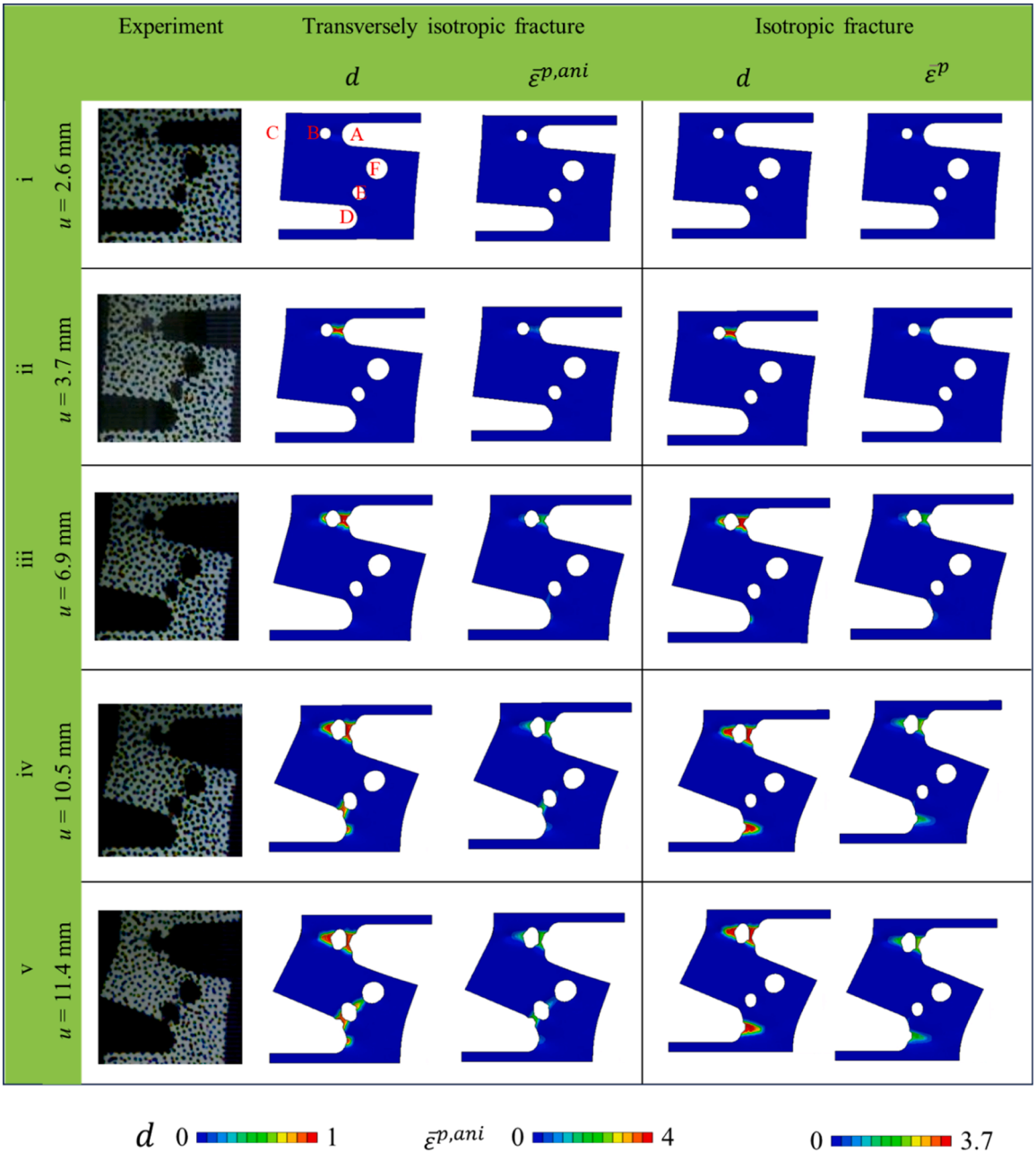

Fig. 15. Experimental and numerical comparison of the modified second Sandia fracture challenge. To reproduce the experiment crack path, it is necessary to consider transversely isotropic fracture initiation in the phase field model. Otherwise, the crack path could be predicted incorrectly.

cracks could be properly predicted. Fracture mechanism analysis found that compression shear and shear were the dominant stress states to trigger damage initiation. This study contributes to an explicit phase field model enriched by strain rate, stress state and orientation dependent constitutive relations, which has been validated by extensive experimental data.

Note that uncertainties significantly influence crack initiation and propagation in 3D-printed metals (Li et al., 2023) primarily due to geometric imperfections and residual stress. A stochastic finite element framework (Feng et al., 2023; Gerasimov et al., 2020) and recently developed deep energy method (Goswami et al., 2020; Samaniego et al., 2020) offer promising approach to effectively address these uncertainties, which will be explored in future work.

CRediT authorship contribution statement

Cunyi Li: Writing – original draft, Visualization, Software, Methodology, Formal analysis, Data curation. **Jian Liu:** Resources,

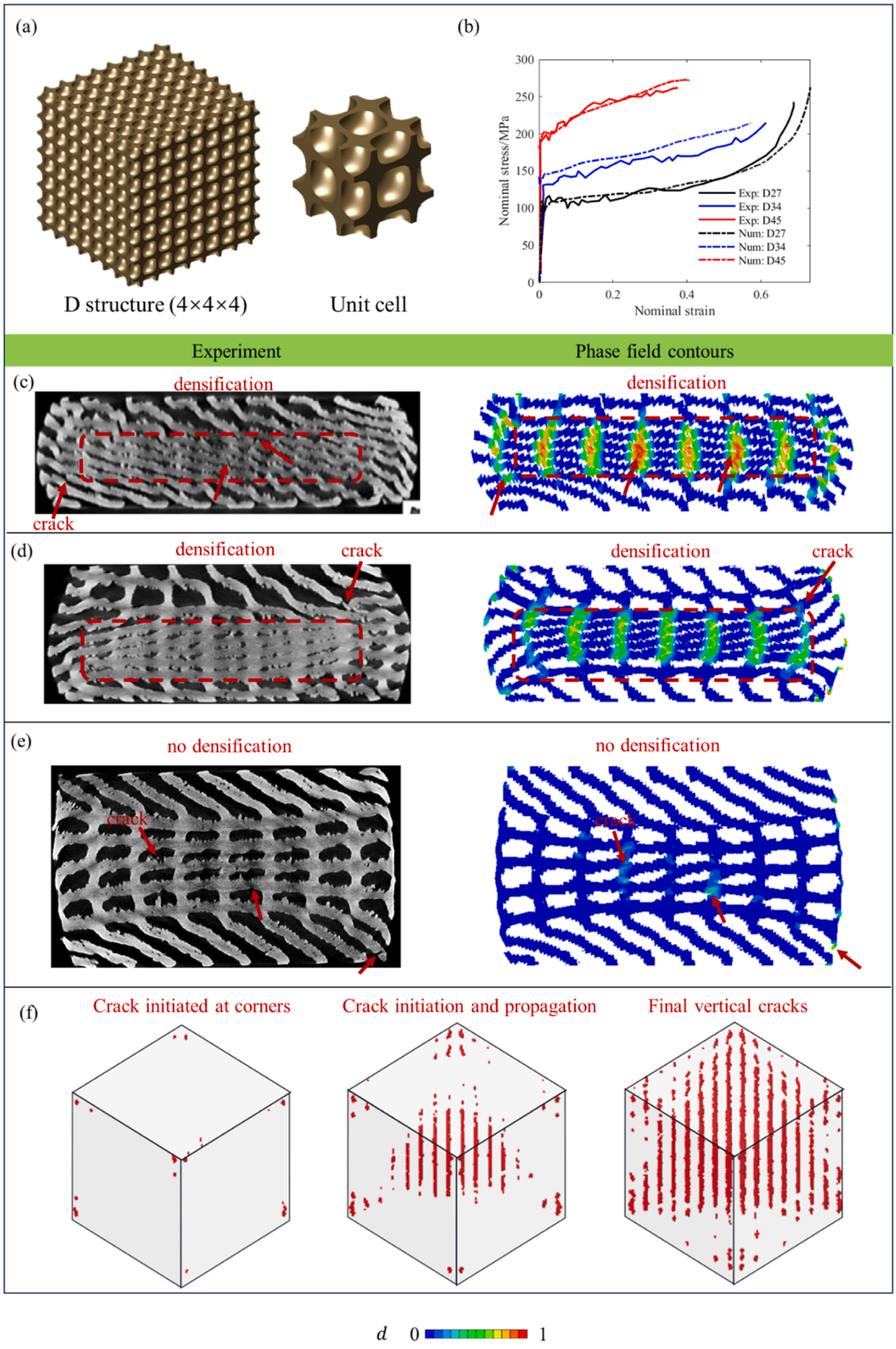

Fig. 16. Simulation of D structures subject to impact loading. (a) The D structure was comprised of a 4 × 4 × 4 array of unit cells, with length of unit cell being 4 mm. The relative volume fractions were 27%, 34%, and 45%. (b) Nominal stress-strain curves for different volume fractions. Simulated fracture patterns of D structure with volume fractions of (c) 27%, (d) 34%, and (e) 45% and experimental data of X-ray CT images (Santiago et al., 2023), suggesting that deformation modes and cracks were well predicted. (f) 3D crack evolution of D structure with volume fraction of 27% in the undeformed configuration, exhibiting distributed cracks over the whole structure.

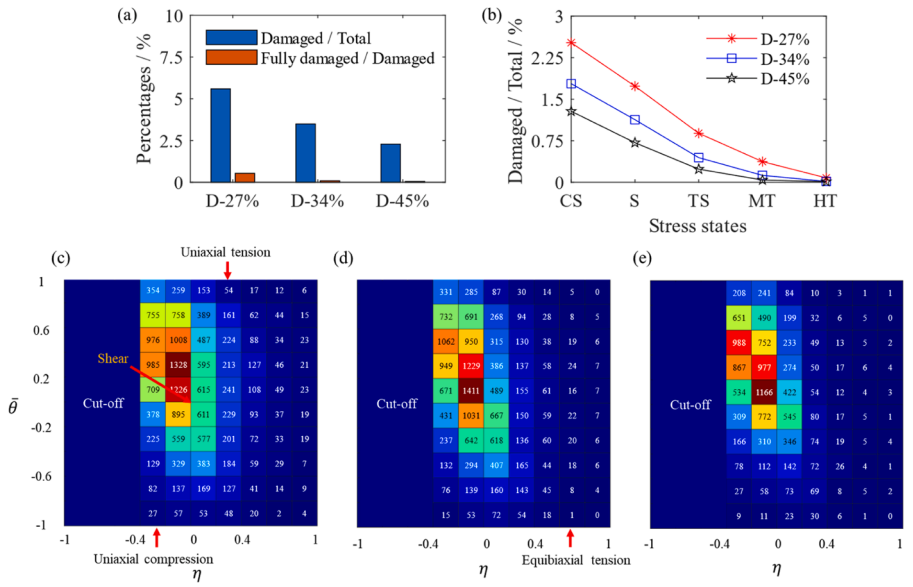

Fig. 17. Statistics of damaged material points for D structures. (a) percentages of partially damaged and fully ruptured material points; (b) percentage of stress states (stress triaxiality) to trigger the damage initiation. CS, S, TS, MT, and HT represent compression-shear, shear, tension-shear, medium stress triaxiality tension, and high stress triaxiality tension, respectively. Heatmaps of stress states (stress triaxiality and Lode angle parameter) at the instant of damage initiation of D structure with volume fractions of (c) 27%, (d) 34%, and (e) 45%. Numbers indicate the numbers of elements falling within the stress state ranges.

Investigation, Funding acquisition. **Le Dong:** Investigation, Data curation. **Chi Wu:** Investigation, Data curation. **Grant Steven:** Writing – review & editing, Supervision, Funding acquisition. **Qing Li:** Writing – review & editing, Supervision, Funding acquisition. **Jianguang Fang:** Writing – review & editing, Supervision, Project administration, Methodology, Funding acquisition, Conceptualization.

Declaration of competing interest

The authors declare that they have no known competing financial interests or personal relationships that could have appeared to influence the work reported in this paper.

Acknowledgments

The support from the Australian Research Council (ARC) Discovery scheme (Grant No. DP190103752) is acknowledged. The first author is a recipient of the FEIT Scholarship and IRS Scholarship at the University of Technology Sydney. The last author is a recipient of the ARC Discovery Early Career Research Award (Grant No. DE210101676). The financial support from the Natural Science Foundation of Guangdong Province (Grant No. 2024A1515011278) is also appreciated.

Data availability

Data will be made available on request.

References

Abrari Vajari, S., Neuner, M., Arunachala, P.K., Ziccarelli, A., Deierlein, G., Linder, C., 2022. A thermodynamically consistent finite strain phase field approach to ductile fracture considering multi-axial stress states. Computer Methods in Applied Mechanics and Engineering 400.

Alessi, R., Marigo, J.J., Maurini, C., Vidoli, S., 2018. Coupling damage and plasticity for a phase-field regularisation of brittle, cohesive and ductile fracture: One-dimensional examples. International Journal of Mechanical Sciences 149, 559–576.

AlMahri, S., Santiago, R., Lee, D.W., Ramos, H., Alabdouli, H., Alteneiji, M., Guan, Z.W., Cantwell, W., Alves, M., 2021. Evaluation of the dynamic response of triply periodic minimal surfaces subjected to high strain-rate compression. Additive Manufacturing 46.

Ambati, M., Gerasimov, T., De Lorenzis, L., 2014. A review on phase-field models of brittle fracture and a new fast hybrid formulation. Computational Mechanics 55, 383–405.

Ambati, M., Gerasimov, T., De Lorenzis, L., 2015. Phase-field modeling of ductile fracture. Computational Mechanics 55, 1017–1040.

Amor, H., Marigo, J.J., Maurini, C., 2009. Regularized formulation of the variational brittle fracture with unilateral contact: Numerical experiments. Journal of the Mechanics and Physics of Solids 57, 1209–1229.

Areias, P., Pinto da Costa, A., Rabczuk, T., Queirós de Melo, F.J.M., Dias-da-Costa, D., Bezzeghoud, M., 2013. An alternative formulation for quasi-static frictional and cohesive contact problems. Computational Mechanics 53, 807–824.

Areias, P., Vu-Bac, N., Rabczuk, T., 2016. A multisurface constitutive model for highly cross-linked polymers with yield data obtained from molecular dynamics simulations. International Journal of Mechanics and Materials in Design 14, 21–36.
Bai, Y., Wierzbicki, T., 2009. Application of extended Mohr–Coulomb criterion to ductile fracture. International Journal of Fracture 161, 1–20.
Bai, Y.L., Wierzbicki, T., 2008. A new model of metal plasticity and fracture with pressure and Lode dependence. International Journal of Plasticity 24, 1071–1096.
Banabic, D., 2010. Sheet Metal Forming Processes Constitutive Modelling and Numerical Simulation. Springer Science & Business Media.
Bao, Y.B., Wierzbicki, T., 2004. On fracture locus in the equivalent strain and stress triaxiality space. International Journal of Mechanical Sciences 46, 81–98.
Belytschko, T., Liu, W.K., Moran, B., Elkhodary, K., 2014. Nonlinear Finite Elements for Continua and Structures. john wiley & sons ltd.
Borden, M.J., Verhoosel, C.V., Scott, M.A., Hughes, T.J.R., Landis, C.M., 2012. A phase-field description of dynamic brittle fracture. Computer Methods in Applied Mechanics and Engineering 217, 77–95.
Borges, C.S.P., Nunes, P.D.P., Akhavan-Safar, A., Marques, E.A.S., Carbas, R.J.C., Alfonso, L., Silva, L.F.M., 2020. A strain rate dependent cohesive zone element for mode I modeling of the fracture behavior of adhesives. Proceedings of the Institution of Mechanical Engineers Part L-Journal of Materials-Design and Applications 234, 610–621.
Bourdin, B., Francfort, G.A., Marigo, J.J., 2000. Numerical experiments in revisited brittle fracture. Journal of the Mechanics and Physics of Solids 48, 797–826.
Bourdin, B., Francfort, G.A., Marigo, J.J., 2008. The variational approach to fracture. Journal of Elasticity 91, 5–148.
Brepols, T., Vladimirov, I.N., Reese, S., 2014. Numerical comparison of isotropic hypo- and hyperelastic-based plasticity models with application to industrial forming processes. International Journal of Plasticity 63, 18–48.
Caddell, R.M., Raghava, R.S., Atkins, A.G., 1973. A yield criterion for anisotropic and pressure dependent solids such as oriented polymers. Journal of Materials science 8, 1641–1646.
Carroll, B.E., Palmer, T.A., Beese, A.M., 2015. Anisotropic tensile behavior of Ti-6Al-4V components fabricated with directed energy deposition additive manufacturing. Acta Materialia 87, 309–320.
Chen, J.S., Pan, S.H., 2012. A Survey on Soc Complementarity Functions and Solution Methods for Socps and Soccps. Pacific Journal of Optimization 8, 33–74.
Chu, D.Y., Li, X., Liu, Z.L., Cheng, J.B., Wang, T., Li, Z.J., Zhuang, Z., 2019. A unified phase field damage model for modeling the brittle-ductile dynamic failure mode transition in metals. Engineering Fracture Mechanics 212, 197–209.
Cui, C.J., Ma, R.J., Martínez-Pañeda, E., 2021. A phase field formulation for dissolution-driven stress corrosion cracking. Journal of the Mechanics and Physics of Solids 147.
Dean, A., Reinoso, J., Jha, N.K., Mahdi, E., Rolfes, R., 2020. A phase field approach for ductile fracture of short fibre reinforced composites. Theoretical and Applied Fracture Mechanics 106.
Deshpande, V.S., Fleck, N.A., Ashby, M.F., 2001. Effective properties of the octet-truss lattice material. Journal of the Mechanics and Physics of Solids 49, 1747–1769.
Dittmann, M., Aldakheel, F., Schulte, J., Schmidt, F., Krüger, M., Wriggers, P., Hesch, C., 2020. Phase-field modeling of porous-ductile fracture in non-linear thermo-elasto-plastic solids. Computer Methods in Applied Mechanics and Engineering 361.
Feng, Y., Wu, D., Stewart, M.G., Gao, W., 2023. Past, current and future trends and challenges in non-deterministic fracture mechanics: A review. Computer Methods in Applied Mechanics and Engineering 412.
Francfort, G.A., Marigo, J.J., 1998. Revisiting brittle fracture as an energy minimization problem. Journal of the Mechanics and Physics of Solids 46, 1319–1342.
Gerasimov, T., Römer, U., Vondrejc, J., Matthies, H.G., De Lorenzis, L., 2020. Stochastic phase-field modeling of brittle fracture: Computing multiple crack patterns and their probabilities. Computer Methods in Applied Mechanics and Engineering 372.
Goswami, S., Anitescu, C., Chakraborty, S., Rabczuk, T., 2020. Transfer learning enhanced physics informed neural network for phase-field modeling of fracture. Theoretical and Applied Fracture Mechanics 106.
Gupta, A., Krishnan, U.M., Mandal, T.K., Chowdhury, R., Nguyen, V.P., 2022. An adaptive mesh refinement algorithm for phase-field fracture models: Application to brittle, cohesive, and dynamic fracture. Computer Methods in Applied Mechanics and Engineering 399.
Hageman, T., Martínez-Pañeda, E., 2023. A phase field-based framework for electro-chemo-mechanical fracture: Crack-contained electrolytes, chemical reactions and stabilisation. Computer Methods in Applied Mechanics and Engineering 415.
Hill, R., 1948. A Theory of the Yielding and Plastic Flow of Anisotropic Metals. Proceedings of the Royal Society of London Series a-Mathematical and Physical Sciences 193, 281–297.
Hofacker, M., Miehe, C., 2012a. Continuum phase field modeling of dynamic fracture: variational principles and staggered FE implementation. International Journal of Fracture 178, 113–129.
Hofacker, M., Miehe, C., 2012b. A Phase Field Model for Ductile to Brittle Failure Mode Transition. Pamm 12, 173–174.
Hofacker, M., Miehe, C., 2013. A phase field model of dynamic fracture: Robust field updates for the analysis of complex crack patterns. International Journal for Numerical Methods in Engineering 93, 276–301.
Huber, W., Asle Zaeem, M., 2023. A mixed mode phase-field model of ductile fracture. Journal of the Mechanics and Physics of Solids 171.
Hughes, T.J.R., Winget, J., 1980. Finite Rotation Effects in Numerical-Integration of Rate Constitutive-Equations Arising in Large-Deformation Analysis. International Journal for Numerical Methods in Engineering 15, 1862–1867.
Jackiewicz, J., 2011. Use of a modified Gurson model approach for the simulation of ductile fracture by growth and coalescence of microvoids under low, medium and high stress triaxiality loadings. Engineering Fracture Mechanics 78, 487–502.
Jin, Y.M., Li, Z.Z., Zhang, H., Shi, Y.L., 2023. A globally convergent smoothing Newton method for the second order cone complementarity approach of elastoplasticity problems. Computers and Geotechnics 156.
Johnson, G.R., Cook, W.H., 1985. Fracture characteristics of three metals subjected to various strains, strain rates, temperatures and pressures. Engineering fracture mechanics 21, 31–48.
Jones, N., 2011. Structural impact. Cambridge university press.
Kang, L., Ge, H.B., Fang, X., 2016. An improved ductile fracture model for structural steels considering effect of high stress triaxiality. Construction and Building Materials 115, 634–650.
Karma, A., Kessler, D.A., Levine, H., 2001. Phase-field model of mode III dynamic fracture. Phys Rev Lett 87, 045501.
Kim, N.-H., 2014. Introduction to nonlinear finite element analysis. Springer Science & Business Media.
Kok, Y., Tan, X.P., Wang, P., Nai, M.L.S., Loh, N.H., Liu, E., Tor, S.B., 2018. Anisotropy and heterogeneity of microstructure and mechanical properties in metal additive manufacturing: A critical review. Materials & Design 139, 565–586.
Komori, K., 2021. Simulation of the influence of Lode parameter on ductile fracture using an ellipsoidal void model. International Journal of Solids and Structures 229.
Kristensen, P.K., Niordson, C.F., Martínez-Pañeda, E., 2020. A phase field model for elastic-gradient-plastic solids undergoing hydrogen embrittlement. Journal of the Mechanics and Physics of Solids 143, 104093.
Kumar, A., Bourdin, B., Francfort, G.A., Lopez-Pamies, O., 2020. Revisiting nucleation in the phase-field approach to brittle fracture. Journal of the Mechanics and Physics of Solids 142.
Li, C.Y., Fang, J.G., Qiu, N., Wu, C., Steven, G., Li, Q., 2024. On fracture mechanism of additively manufactured triply periodic minimal surface structures using an explicit phase field model. Additive Manufacturing 86.
Li, C.Y., Fang, J.G., Wan, Y.H., Qiu, N., Steven, G., Li, Q., 2023. Phase field fracture model for additively manufactured metallic materials. International Journal of Mechanical Sciences 251, 108324.
Li, C.Y., Fang, J.G., Wu, C., Sun, G.Y., Steven, G., Li, Q., 2022a. Phase field fracture in elasto-plastic solids: Incorporating phenomenological failure criteria for ductile materials. Computer Methods in Applied Mechanics and Engineering 391, 114580.
Li, H., Fu, M.W., Lu, J., Yang, H., 2011. Ductile fracture: Experiments and computations. International Journal of Plasticity 27, 147–180.
Li, J.N., Gao, D., Lu, Y., Hao, Z.P., Wang, Z.Q., 2022b. Mechanical properties and microstructure evolution of additive manufactured 316L stainless steel under dynamic loading. Materials Science and Engineering a-Structural Materials Properties Microstructure and Processing 855.

Li, X.Y., Roth, C.C., Tancogne-Dejean, T., Mohr, D., 2020a. Rate- and temperature-dependent plasticity of additively manufactured stainless steel 316L: Characterization, modeling and application to crushing of shell-lattices. International Journal of Impact Engineering 145, 103671.
Li, X.Y., Roth, C.C., Tancogne-Dejean, T., Mohr, D., 2020b. Rate- and temperature-dependent plasticity of additively manufactured stainless steel 316L: Characterization, modeling and application to crushing of shell-lattices. International Journal of Impact Engineering 145.
Li, Z., Voisin, T., McKeown, J.T., Ye, J.C., Braun, T., Kamath, C., King, W.E., Wang, Y.M., 2019. Tensile properties, strain rate sensitivity, and activation volume of additively manufactured 316L stainless steels. International Journal of Plasticity 120, 395–410.
Liu, J., Dong, L., Li, C., Fang, J., Chen, Y., Cui, J., 2024. Quasi-static and dynamic tensile behaviour of 316L stainless steels: Rolled versus laser-powder bed fusion (LPBF) fabricated samples. International Journal of Impact Engineering 190, 104972.
Liu, Y.Y., Feng, Y., Wu, D., Chen, X.J., Gao, W., 2023. Virtual modelling integrated phase field method for dynamic fracture analysis. International Journal of Mechanical Sciences 252.
Lo, Y.-S., Hughes, T.J.R., Landis, C.M., 2023. Phase-field fracture modeling for large structures. Journal of the Mechanics and Physics of Solids 171.
Loew, P.J., Peters, B., Beex, L.A.A., 2019. Rate-dependent phase-field damage modeling of rubber and its experimental parameter identification. Journal of the Mechanics and Physics of Solids 127, 266–294.
Lou, Y.S., Yoon, J.W., 2017. Anisotropic ductile fracture criterion based on linear transformation. International Journal of Plasticity 93, 3–25.
Lou, Y.S., Yoon, J.W., Huh, H., 2014. Modeling of shear ductile fracture considering a changeable cut-off value for stress triaxiality. International Journal of Plasticity 54, 56–80.
Luo, M., Dunand, M., Mohr, D., 2012. Experiments and modeling of anisotropic aluminum extrusions under multi-axial loading - Part II: Ductile fracture. International Journal of Plasticity 32-33, 36–58.
Luscher, D.J., Buechler, M.A., Walters, D.J., Bolme, C.A., Ramo, K.J., 2018. On computing the evolution of temperature for materials under dynamic loading. International Journal of Plasticity 111, 188–210.
Marandi, S.M., Badnava, H., Dehkordi, M.B., Nourbakhsh, S.H., 2021. Phase-field modeling of coupled anisotropic plasticity-ductile fracture in rate-dependent solids. Journal of the Brazilian Society of Mechanical Sciences and Engineering 43.
Marandi, S.M., Nourbakhsh, S.H., Dehkordi, M.B., Badnava, H., 2020. Finite element implementation of coupled temperature-rate dependent fracture using the phase field model. Mechanics of Materials 148.
Margerit, P., Weisz-Patrault, D., Ravi-Chandar, K., Constantinescu, A., 2021. Tensile and ductile fracture properties of as-printed 316L stainless steel thin walls obtained by directed energy deposition. Additive Manufacturing 37.
Miehe, C., Aldakheel, F., Raina, A., 2016. Phase field modeling of ductile fracture at finite strains: A variational gradient-extended plasticity-damage theory. International Journal of Plasticity 84, 1–32.
Miehe, C., Hofacker, M., Schänzel, L.M., Aldakheel, F., 2015. Phase field modeling of fracture in multi-physics problems. Part II. Coupled brittle-to-ductile failure criteria and crack propagation in thermo-elastic-plastic solids. Computer Methods in Applied Mechanics and Engineering 294, 486–522.
Miehe, C., Hofacker, M., Welschinger, F., 2010a. A phase field model for rate-independent crack propagation: Robust algorithmic implementation based on operator splits. Computer Methods in Applied Mechanics and Engineering 199, 2765–2778.
Miehe, C., Welschinger, F., Hofacker, M., 2010b. Thermodynamically consistent phase-field models of fracture: Variational principles and multi-field FE implementations. International Journal for Numerical Methods in Engineering 83, 1273–1311.
Molnár, G., Gravouil, A., Seghir, R., Réthoré, J., 2020. An open-source Abaqus implementation of the phase-field method to study the effect of plasticity on the instantaneous fracture toughness in dynamic crack propagation. Computer Methods in Applied Mechanics and Engineering 365, 113004.
Noii, N., Khodadadian, A., Ulloa, J., Aldakheel, F., Wick, T., François, S., Wriggers, P., 2021. Bayesian inversion for unified ductile phase-field fracture. Computational Mechanics 68, 943–980.
Pack, K., Luo, M., Wierzbicki, T., 2014. Sandia Fracture Challenge: blind prediction and full calibration to enhance fracture predictability. International Journal of Fracture 186, 155–175.
Pandya, K.S., Roth, C.C., Mohr, D., 2020. Strain rate and temperature dependent fracture of aluminum alloy 7075: Experiments and neural network modeling. International Journal of Plasticity 135.
Peng, Z.L., Zhao, H.S., Li, X., 2021. New ductile fracture model for fracture prediction ranging from negative to high stress triaxiality. International Journal of Plasticity 145.
Pijaudier-Cabot, G., Bažant, Z.P., Tabbara, M., 1988. Comparison of various models for strain-softening. Engineering computations.
Ren, H.L., Zhuang, X.Y., Anitescu, C., Rabczuk, T., 2019. An explicit phase field method for brittle dynamic fracture. Computers & Structures 217, 45–56.
Roth, C.C., Mohr, D., 2014. Effect of strain rate on ductile fracture initiation in advanced high strength steel sheets: Experiments and modeling. International Journal of Plasticity 56, 19–44.
Samaniego, E., Anitescu, C., Goswami, S., Nguyen-Thanh, V.M., Guo, H., Hamdia, K., Zhuang, X., Rabczuk, T., 2020. An energy approach to the solution of partial differential equations in computational mechanics via machine learning: Concepts, implementation and applications. Computer Methods in Applied Mechanics and Engineering 362.
Santiago, R., Ramos, H., AlMahri, S., Banabila, O., Alabdouli, H., Lee, D.W., Aziz, A., Rajput, N., Alves, M., Guan, Z.W., 2023. Modelling and optimisation of TPMS-based lattices subjected to high strain-rate impact loadings. International Journal of Impact Engineering 177.
Shen, R.L., Waisman, H., Guo, L.C., 2019. Fracture of viscoelastic solids modeled with a modified phase field method. Computer Methods in Applied Mechanics and Engineering 346, 862–890.
Simo, J.C., Hughes, T.J., 2006. Computational inelasticity. Springer Science & Business Media.
Smith, W.L., Roehling, J.D., Strantza, M., Ganeriwala, R.K., Ashby, A.S., Vrancken, B., Clausen, B., Guss, G.M., Brown, D.W., McKeown, J.T., Hill, M.R., Matthews, M. J., 2021. Residual stress analysis of in situ surface layer heating effects on laser powder bed fusion of 316L stainless steel. Additive Manufacturing 47.
Somlo, K., Frodal, B.H., Funch, C.V., Poulios, K., Winther, G., Hopperstad, O.S., Borvik, T., Niordson, C.F., 2022. Anisotropic yield surfaces of additively manufactured metals simulated with crystal plasticity. European Journal of Mechanics a-Solids 94.
Tang, J., He, M.C., Qiao, Y.F., Xia, M., Tao, Z.G., 2021. Tensile behavior of a novel high-strength and high-toughness steel at strain rates from 0.1 s to 1000 s. Construction and Building Materials 304.
Wang, T., Ye, X., Liu, Z.L., Chu, D.Y., Zhuang, Z., 2019. Modeling the dynamic and quasi-static compression-shear failure of brittle materials by explicit phase field method. Computational Mechanics 64, 1537–1556.
Wang, Y.P., Chen, X.Z., Xiao, X.K., Vershinin, V.V., Ge, R.C., Li, D.S., 2020. Effect of Lode angle incorporation into a fracture criterion in predicting the ballistic resistance of 2024-T351 aluminum alloy plates struck by cylindrical projectiles with different nose shapes. International Journal of Impact Engineering 139.
Wang, Y.T., Borja, R.I., Wu, W., 2023. Dynamic strain localization into a compaction band via a phase-field approach. Journal of the Mechanics and Physics of Solids 173.
Weinberg, K., Wieners, C., 2022. Dynamic phase-field fracture with a first-order discontinuous Galerkin method for elastic waves. Computer Methods in Applied Mechanics and Engineering 389.
Wilson-Heid, A.E., Qin, S.P., Beese, A.M., 2020. Multiaxial plasticity and fracture behavior of stainless steel 316L by laser powder bed fusion: Experiments and computational modeling. Acta Materialia 199, 578–592.
Wu, J.-Y., Nguyen, V.P., Nguyen, C.T., Sutula, D., Sinaie, S., Bordas, S.P., 2020. Phase-field modeling of fracture. Advances in applied mechanics 53, 1–183.
Wu, J.Y., 2017. A unified phase-field theory for the mechanics of damage and quasi-brittle failure. Journal of the Mechanics and Physics of Solids 103, 72–99.
Wu, J.Y., Nguyen, V.P., 2018. A length scale insensitive phase-field damage model for brittle fracture. Journal of the Mechanics and Physics of Solids 119, 20–42.
Xiao, X.K., Pan, H., Bai, Y.L., Lou, Y.S., Lin, C., 2019. Application of the modified Mohr-Coulomb fracture criterion in predicting the ballistic resistance of 2024-T351 aluminum alloy plates impacted by blunt projectiles. International Journal of Impact Engineering 123, 26–37.
Zhang, Z.J., Qiu, Y.S., Hu, Z.Q., Ye, H.F., Zhang, H.W., Zheng, Y.G., 2022. Explicit phase-field total Lagrangian material point method for the dynamic fracture of hyperelastic materials. Computer Methods in Applied Mechanics and Engineering 398.

Zhou, X., Lu, D., Zhang, Y., Du, X., Rabczuk, T., 2022. An open-source unconstrained stress updating algorithm for the modified Cam-clay model. Computer Methods in Applied Mechanics and Engineering 390.
Zhuang, X., Zhou, S., Huynh, G.D., Areias, P., Rabczuk, T., 2022. Phase field modeling and computer implementation: A review. Engineering Fracture Mechanics 262.
Ziaei-Rad, V., Shen, Y.X., 2016. Massive parallelization of the phase field formulation for crack propagation with time adaptivity. Computer Methods in Applied Mechanics and Engineering 312, 224–253.